

Relativistic Tidal Disruption in Black Hole and Wormhole Backgrounds

Pritam Banerjee*

Indian Institute of Astrophysics, Koramangala, Bangalore 560034, India

Kowsona Chakraborty,[†] Niles Mondal,[‡] and Tapobrata Sarkar[§]

Department of Physics, Indian Institute of Technology Kanpur, Kanpur 208016, India

Abstract

Black holes (BHs) and wormholes (WHs) are characterized by distinct spacetime geometries, whose differences become pronounced close to the central objects. A useful way to probe such differences is via the dynamics of stellar tidal disruption events in the regime of strong gravity. Here, using a general relativistic smoothed particle hydrodynamics code inspired from an algorithm developed by Liptai and Price, we perform a suite of numerical simulations of solar mass polytropic stars in the background of supermassive Schwarzschild BHs and similar mass exponential WHs. Important differences between the two geometries near the BH event horizon or the WH throat is provided by the distinct outcomes of such events. For a given impact parameter, BH backgrounds lead to greater tidal stripping compared to WHs ones and further, the critical impact parameter, beyond which the star undergoes full tidal disruption is higher for WH backgrounds compared to BHs. We further study the differences in observable peak fallback rates in the two backgrounds. We also provide a quantitative explanation for the tendency of stars in partial tidal disruptions to retain larger cores around more massive centers, by computing tidal stresses in a Fermi normal coordinate system and introducing an appropriate measure of stellar compactness. Finally, we suggest a way to observationally distinguish BH and WH backgrounds, based on the properties of different observables.

arXiv:2603.26442v1 [astro-ph.HE] 27 Mar 2026

* bpritamphy@gmail.com

† kowsonac24@iitk.ac.in

‡ nilesm24@iitk.ac.in

§ tapo@iitk.ac.in

I. INTRODUCTION

A. Motivation and summary

The study of massive compact astrophysical objects with or without an event horizon remains one of the most active areas of research in theories of gravity. The tidal forces they produce can fully or partially destroy a smaller object, such as a star, that comes sufficiently close. Such events, called tidal disruption events (TDEs) [1–7] provide a powerful observational probe into the strong gravitational regime of massive compact objects. In this context, it is common to model the massive object as a Black Hole (BH), and indeed there is abundant literature by now on TDEs involving stellar objects and Schwarzschild or Kerr BHs (for recent reviews see the collection of articles in [8]), inspired by the fact that supermassive BHs with masses $M_{\bullet} \sim 10^6 - 10^{10} M_{\odot}$ are by now believed to exist at the center of most galaxies (see, e.g., the reviews [9–11]). In the last few decades, TDEs have been extensively studied both analytically and numerically, and is an ideal theoretical laboratory to understand the physics of luminous electromagnetic transients that result from them. Further, TDEs are also probes of theories of gravity via accretion physics and stellar dynamics. In a TDE, a star approaching a BH is disrupted near the tidal radius, and produces a stream of debris that might have complicated dynamics due to various competing forces acting on it. Depending on the nature of the TDE, a part of the debris falls back into the BH over time, and this generates a characteristic light curve whose behaviour encodes both the stellar structure and the nature of the BH (for a small sampling of the literature see [12–18]).

While TDEs by BHs are believed to be a common phenomenon near galactic centers, the literature on tidal disruption by horizonless compact objects is relatively rarer. This fact assumes importance, as currently there is no direct empirical observation of the event horizon, neither is there an accepted proof of the cosmic censorship conjecture. An example of such an exotic object is the wormhole (WH), a geometry which contains a throat that connects two different universes or two distant regions of a single universe. WHs continue to remain a subject of interest long after they were first proposed as a manifestation of a nontrivial change in the topology of spacetime [19], and early efforts to explain their possible emergence through cosmological phase transitions were undertaken in [20–22]. A WH is said to be traversable if physical observers or signals can pass through its throat. The authors of [23] showed that the Schwarzschild WH (called the Einstein–Rosen bridge) does not satisfy this criterion. A traversable WH geometry was obtained in [24], and this work was soon followed by proposals for constructing a “time machine” based on such geometries [25, 26]. A comprehensive discussion of these developments can be found in the monograph by [27] (see also [28] for additional related work). Also, it is well established that the matter sources required to sustain WH spacetimes generally violate the

standard energy conditions of general relativity [24], the so called “exotic matter.” Nonetheless, a variety of approaches have been explored to avoid these violations, in particular, time-dependent WH solutions [29] and modified gravity theories [30] are known to provide frameworks in which WH configurations may be realised without violating energy conditions.

Apart from purely theoretical reasons, our main interest in WH spacetimes is due to the fact that these are BH mimickers. For example, [31] pointed out that several features of BH spacetimes can be closely resembled by WHs as well, such as quasi-normal modes, accretion properties, no hair theorems, lensing features, etc. (see, e.g., [32, 33]). This fact assumes importance in the context of the previous discussion as far as astrophysical observations involving TDEs are concerned. Namely, we ask if (and to what extent) TDEs in BH and WH backgrounds are similar, and if there is a way to observationally differentiate between these two spacetimes. In a previous paper [34], we explored this question via some “static” properties of TDEs in the two different backgrounds. Namely, we showed that although at large distances both BHs and WHs are expected to behave like Newtonian objects, as one goes closer to the event horizon of the BH or the WH throat, different tidal effects on stars can be seen, due to the different geometries. There we quantified this difference by a numerical procedure by transforming to a local Fermi-normal (FN) tetrad basis and solving the stellar hydrostatic equations in this basis following the earlier work of [35] (see also [36–38]). This analysis focused on the computation of a minimum central density below which a star would be tidally disrupted, from which a critical mass could be obtained. Now, the tidal radius computed by equating the tidal force on a star due to a massive object with mass M_\bullet with its self gravity at the surface gives an estimate of the closest radial distance that the star can come near the massive object without getting tidally disrupted, and is given by

$$r_t = R_* (M_\bullet/M_*)^{1/3} \quad , \quad (1)$$

with M_* and R_* denoting the mass and radius of the star, respectively. In [34], the critical mass mentioned above was used to cast this relation in the form $r_t/R_* = \alpha (M_\bullet/M_*)^\delta$, with α and δ characterising the variations in BH and WH backgrounds.

Here, we go beyond this method to compute the time dependent dynamics of TDEs in BH and WH backgrounds. This involves numerical simulations of stars in these backgrounds in global coordinates, focusing on observables like fallback rates and gravitational waves. For the numerical analysis, we use a general relativistic smoothed particle hydrodynamics (GRSPH) code developed by us that extends our previous code, whose details appear in [39], and we closely follow the algorithm as described by Liptai and Price [40] (see also [41]). While we will present the results of the simulations in the main text of the paper, the necessary numerical tests establishing the robustness of the code is detailed in Appendix A.

B. The black hole and wormhole gravity backgrounds

To distinguish between BHs and WHs, we will study ultra deep tidal encounters in the regime where General Relativity (GR) plays a major role. To keep the analysis simple, we work with the Schwarzschild BH and Morris-Thorne type exponential WH [24], and compare TDEs in these backgrounds. For both of the cases, the masses are $\sim \mathcal{O}(10^6 - 10^7 M_\odot)$ and the stellar mass and radius is chosen as $1 M_\odot$ and $1 R_\odot$ with polytropic equation of state having $\gamma = 5/3$, so that back-reaction effects can be safely ignored and the BH and WH provide a fixed background geometry. The BH is quantified by the metric

$$ds^2 = - \left(1 - \frac{2GM_\bullet}{c^2 r} \right) c^2 dt^2 + \frac{1}{1 - \frac{2GM_\bullet}{c^2 r}} dr^2 + r^2 d\theta^2 + r^2 \sin^2 \theta d\phi^2, \quad (2)$$

with M_\bullet being its ADM mass and G and c denote the Newton's gravitational constant and the speed of light, respectively. On the other hand, the quintessential example of a static traversable WH of the Morris-Thorne type is provided by the metric written in the same coordinates,

$$ds^2 = -e^{2\Phi(r)} c^2 dt^2 + \frac{1}{1 - \frac{b(r)}{r}} dr^2 + r^2 (d\theta^2 + \sin^2 \theta d\phi^2). \quad (3)$$

The example that we consider here is the exponential WH with

$$e^{2\Phi(r)} = e^{-\frac{2GM_\bullet}{c^2 r}}, \quad b(r) = \frac{2GM_\bullet}{c^2}, \quad (4)$$

where M_\bullet is the ADM mass of the WH. The WH throat is defined by $r_{th} = \frac{2GM_\bullet}{c^2}$. From a Newtonian perspective, an object that is captured by a BH, instead tunnels through the throat of a WH of the same mass. The choice of a constant shape function $b(r)$ results in zero energy density, and the WH spacetime is supported only by tangential and radial pressures. Consequently, there is no matter interaction with the star, making this a somewhat convenient case to compare with vacuum BH. We consider parabolic stellar orbits (with eccentricity $e = 1$) in the background of the BH and WH spacetimes introduced above. The interaction of the star with the background geometry is parametrized by the impact parameter β . Defining the orbital periapsis distance as r_p , this is given by $\beta \equiv r_t/r_p$, with r_t defined in Eq. (1). For a fixed stellar structure, increasing β corresponds to deeper encounters, bringing the star closer to the event horizon $r_s = \frac{2GM_\bullet}{c^2}$ in the BH spacetime, or to the throat r_{th} in the WH spacetime, thereby enhancing GR effects.

We define the critical impact parameter β_c as the threshold separating encounters that leave behind a self-bound stellar remnant (partial disruptions) from those resulting in complete disruptions. For polytropic stars with adiabatic index $\gamma = 5/3$ that we consider here, hydrodynamical simulations have long established that this transition is sharp. Using SPH simulations, [12] first demonstrated that the transition occurs at $\beta_c \simeq 0.9$, a result subsequently confirmed and refined by [42], who obtained

$\beta_c = 0.92 \pm 0.02$. An analytic prescription calibrated against these simulations by [43] yields a slightly higher effective threshold, $\beta_c \simeq 0.95\text{--}0.96$, once differences in the definition of the tidal radius are taken into account. Relativistic studies incorporating BH spacetime curvature show that relativistic tidal enhancement produces only modest shifts in β_c for encounters occurring outside the innermost stable circular orbit [44].

In order to study the differences in BH and WH TDEs, we first fix the regime of interest. Note that from the definition of the impact parameter and using Eq. (1), in units of the gravitational radius $r_g = GM/c^2$, the periapsis distance scales as $\frac{r_p}{r_g} \sim M_\bullet^{-2/3}$. With our choice of stellar parameters, if for example $M_\bullet \sim 10^6 M_\odot$, then with $\beta \sim 1$, the periapsis is found to be $r_p \sim 50r_g$. At such a large distance, both the BH and the WH backgrounds are effectively Newtonian and thus cannot possibly be distinguished by TDEs. With this value of the central mass, we find that $\beta_c \simeq 0.93$ for the BH spacetime (consistent with previous relativistic studies) while the WH spacetime exhibits a slightly higher threshold, $\beta_c \simeq 0.95$, and the difference is thus minor.

For examining genuine relativistic effects due to the two backgrounds, we thus need to consider higher values of the central mass leading to lower $r_p(r_g)$. In this paper, we have chosen to perform numerical simulations with the values of the BH and WH masses ranging from $6 \times 10^6 - 1.2 \times 10^7 M_\odot$, for which r_p varies from $\sim 7 - 15r_g$ and therefore our simulations capture genuine relativistic effects that should be useful in differentiating the nature of tidal dynamics in BH and WH backgrounds.

II. TIDAL TENSOR IN THE RELATIVISTIC REGIME

Since WHs are known to be BH mimickers, a natural question in the light of the above discussion would be to ask if TDEs from WHs look like ones from BHs with a different set of parameters. To this end, it is useful to examine two aspects of TDEs that are most easily studied in the FN co-moving frame of the star, namely the tidal tensor and the spread of energy at the periapsis. To keep the analysis simple, we work in the so called ‘‘tilde frame’’ that is co-rotating with the star [35]. This will be enough to discuss the necessary physics.

We start with the tidal tensor defined as $C_{ij} = R_{\mu\nu\rho\lambda} \hat{e}_0^\mu \hat{e}_i^\nu \hat{e}_0^\rho \hat{e}_j^\lambda = R_{0i0j}$. Here, $R_{\mu\nu\rho\lambda}$ is the Riemann tensor and \hat{e}_k^α denote the usual FN tetrads which are written for parabolic orbits in [34]. Using these, a simple computation yields for our BH and WH backgrounds, the diagonal matrices with components

(evaluated at r_p ; in this section we set $G = c = 1$ to avoid cluttering of notation)

$$C_{ij}^{\text{BH}} = \left\{ -\frac{2M_\bullet(M_\bullet + r_p)}{r_p^3(r_p - 2M_\bullet)}, \frac{M_\bullet(4M_\bullet + r_p)}{r_p^3(r_p - 2M_\bullet)}, \frac{M_\bullet}{r_p^3} \right\},$$

$$C_{ij}^{\text{WH}} = \left\{ -\frac{M_\bullet}{r_p^5} \left(e^{\frac{2M_\bullet}{r_p}} (2M_\bullet^2 - 6M_\bullet r_p + 3r_p^2) + r_p^2 \right), \frac{M_\bullet}{r_p^4} \left(e^{\frac{2M_\bullet}{r_p}} (3r_p - 2M_\bullet) - 2r_p \right), \frac{M_\bullet}{r_p^4} (r_p - 2M_\bullet) \right\} \quad (5)$$

where M_\bullet is the mass of the central object (the BH result appeared previously in [45]). These expressions become identical in the Newtonian limit $r_p \gg M_\bullet$, but clearly there is no simple change of parameters that makes them equivalent at smaller distances. The above expressions show that whereas some of the tidal tensor components diverge near the BH event horizon, they are finite valued near the WH throat. Hence, in this latter region, WHs are not efficient BH mimickers as far as deep tidal encounters are concerned.

This can be further substantiated by the energy spread at the periapsis, that captures the difference in specific energy between the center of mass of the star and a point on its surface, assuming that the star retains its spherical shape at the periapsis. The expression for the energy spread was written in [18] and reads

$$\Delta E = -g_{\mu\nu} \hat{e}_0^\mu \hat{e}_i^\nu \Gamma_{\rho 0}^\nu X^i, \quad (6)$$

where Γ is the Christoffel symbol and X^i denotes the spatial distance measured in the FN coordinates. A straightforward computation yields that at the periapsis,

$$\Delta E^{\text{BH}} = \frac{M_\bullet}{\sqrt{r_p^3(r_p - 2M_\bullet)}} R_*, \quad \Delta E^{\text{WH}} = M_\bullet \sqrt{\frac{r_p - 2M_\bullet}{r_p^5}} R_*. \quad (7)$$

These are identical in the limit $r_p \gg M_\bullet$, but we again see that there is no simple relation that would effectively mimic the energy spread of the WH with that of a BH at smaller values of r_p , namely, ΔE diverges near the BH event horizon, but vanishes near the WH throat.

Now, a Keplerian approximation [15] to the motion of stellar debris after a full TDE is robust even for close encounters as the debris spends most of the time far from the central mass before it returns (approximately) to its initial position. With such an approximation, the time of return of the most bound debris is known to be given by $T = \frac{\pi M_\bullet}{\sqrt{2}} (\Delta E)^{-3/2}$, and hence we have, assuming TDEs at the same r_p and for the same central mass,

$$\frac{T^{\text{BH}}}{T^{\text{WH}}} = \left(1 - \frac{2M_\bullet}{r_p} \right)^{3/2}. \quad (8)$$

Thus, for similar central masses and periapsis distances, $T^{\text{WH}} \gg T^{\text{BH}}$ if r_p is close to $2M_\bullet$. From this we can also conclude that since the peak of the mass fallback rate of the stellar debris into the BH horizon or WH throat can be approximated to be $\dot{M}_{\text{peak}} \sim 1/T$, then we have

$$\frac{\dot{M}_{\text{peak}}^{\text{BH}}}{\dot{M}_{\text{peak}}^{\text{WH}}} = \left(1 - \frac{2M_\bullet}{r_p} \right)^{-3/2}, \quad (9)$$

Implying that the peak fallback rate of debris into the BH will be much higher than that into the WH, for full TDEs with similar parameters. We point out here that the above analysis pertains to full TDEs. For partial TDEs, a FN frame analysis becomes more challenged due to the competing gravity of the central mass and the remnant core, and a more refined approach is usually needed that incorporates stellar hydrodynamics.

From the above discussion, it should be clear that when $r_p \approx$ a few r_g , BHs and WHs should quantitatively differ as far as TDEs are concerned. Such events at such small periapsis distances naturally call for hydrodynamical simulations and we now present our results from these.

III. SIMULATION RESULTS AND OBSERVABLES

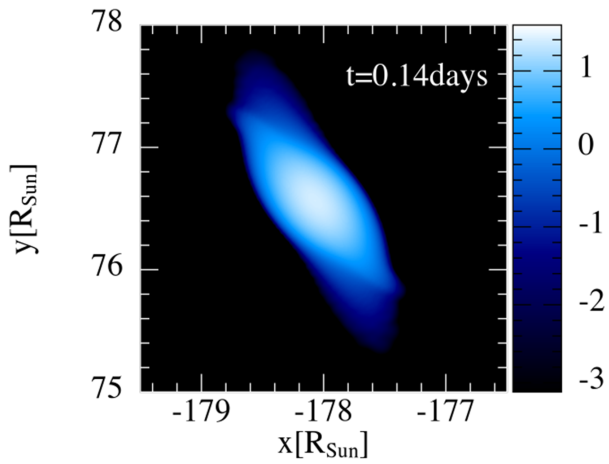
In this section, we present the results of our numerical simulations. These will include both theoretical outcomes of the TDEs as well as observables.

A. Visual differences of stellar density distribution

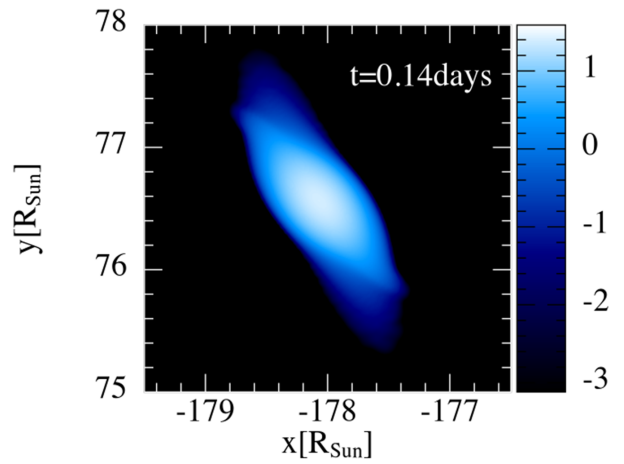
To begin with, it is useful to provide a comparison of the two scenarios. To this end, we show aspects of the remnant core survival with fixed initial parameters. We compare tidal disruption events produced by a BH and an WH, evolved from identical initial stellar and orbital parameters, with a central mass $M_\bullet = 1.2 \times 10^7 M_\odot$, and impact parameter $\beta = 1.3$. Both spacetimes exhibit comparable tidal deformation near periapsis ($t/t_p \simeq 1$). Subsequently, at 0.18 days and 0.55 days, the differences in the two cases are clearly visible. While the BH encounter results in complete destruction of the stellar core (left column of Figure 1), the WH retains a compact, gravitationally bound core (right column of Figure 1).

B. Nature of the bound debris in partial disruptions

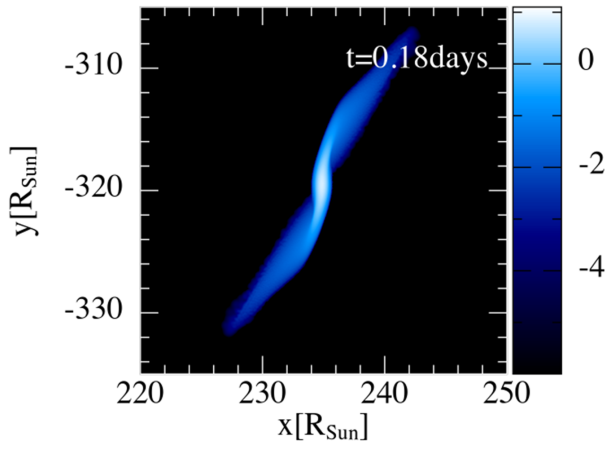
For relatively smaller values of β than those considered above, there is a self-bound core that is left behind after the tidal encounter. The mass of this core is different in BH and WH backgrounds. In Figure 2, we show the behaviour of the self-bound core for two different central masses $6 \times 10^6 M_\odot$ (Figure 2: A and B) and $1.1 \times 10^7 M_\odot$ (Figure 2: C and D) for a few different values of β . It is clearly seen that for partial TDEs, WHs retain significantly higher core mass compared to BHs of the same mass, for a given value of β . On the other hand, in higher β values, BHs produce full disruptions while WHs still preserve cores. This brings us to the issue of the critical impact parameter beyond which a star is disrupted.



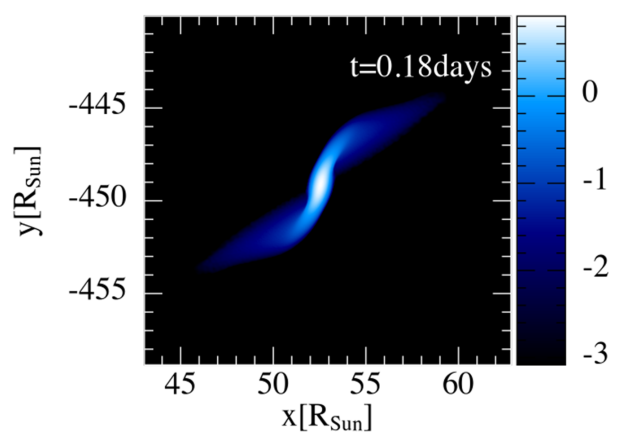
(A) BH: Periapsis



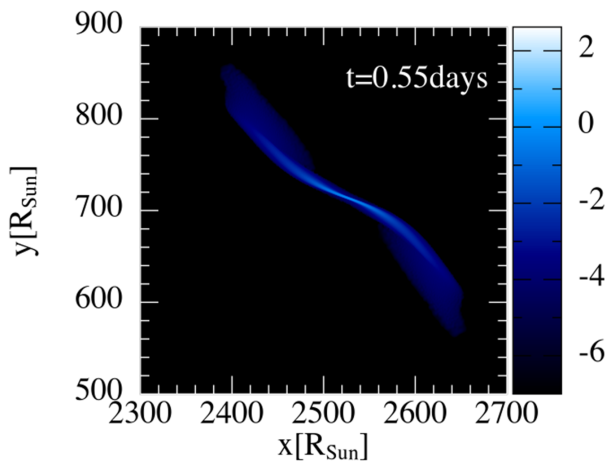
(B) WH: Periapsis



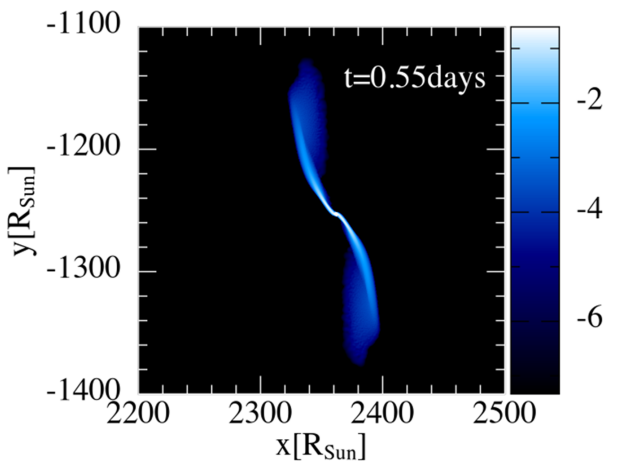
(C) BH: $t = 0.18$ day



(D) WH: $t = 0.18$ day



(E) BH: $t = 0.55$ day



(F) WH: $t = 0.55$ day

FIG. 1: Evolution of debris around BH (left column) and WH (right column) of $1.2 \times 10^7 M_\odot$, $\beta = 1.3$ ($r_p \approx 6.9 r_g$). Log density (in $g\text{ cm}^{-2}$) is shown via the color bar. A remnant self-bound core is visible at $t = 0.55$ days in the WH case (bottom right), indicating partial disruption.

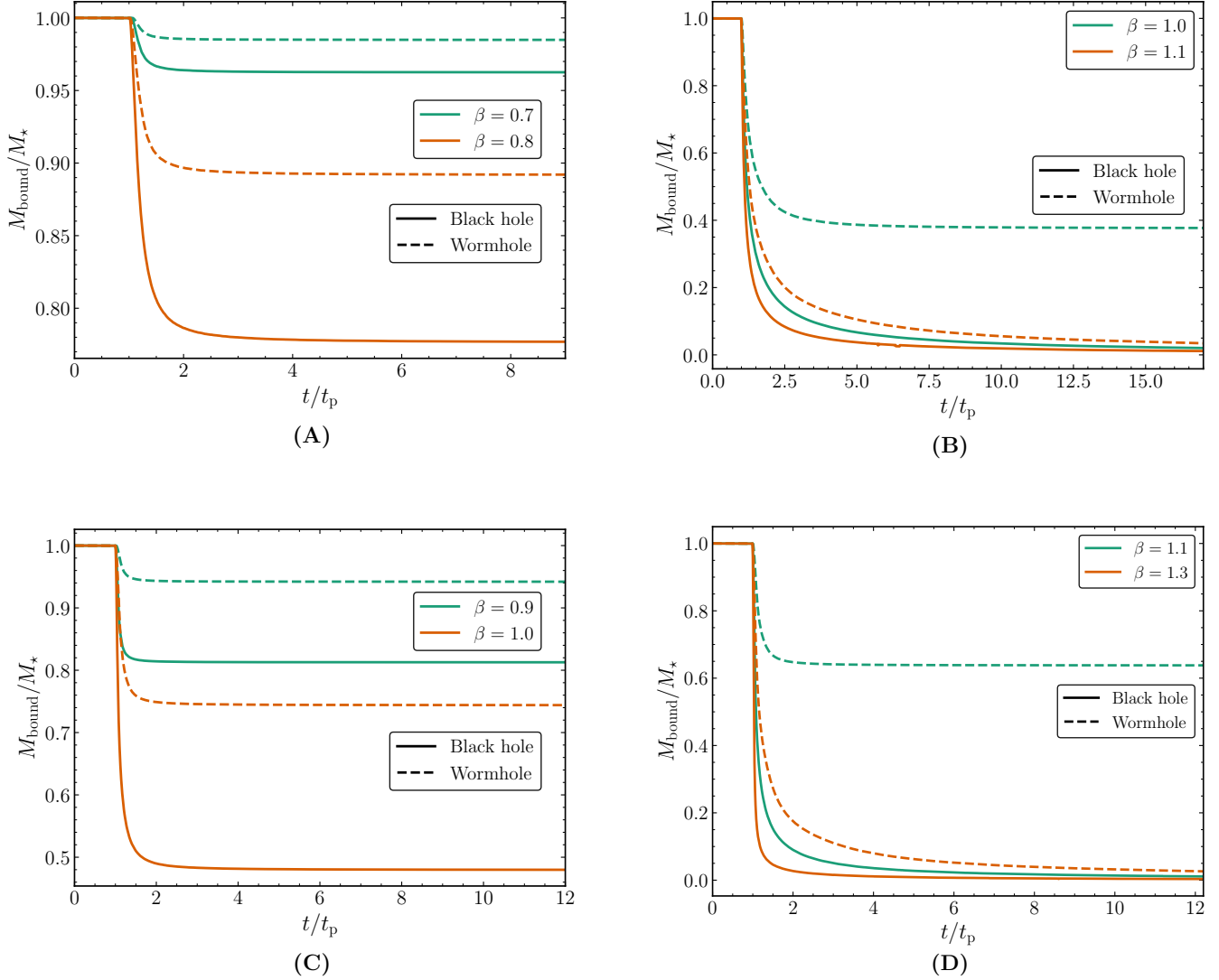


FIG. 2: Bound core mass fraction, M_{bound}/M_* , as a function of periaapsis-normalized time, t/t_p , for BH (solid lines) and WH (dashed lines) encounters. Panels (A) and (B) correspond to $M_\bullet = 6 \times 10^6 M_\odot$, while panels (C) and (D) correspond to $M_\bullet = 1.1 \times 10^7 M_\odot$. Each panel shows two values of the impact parameter β , as indicated in the legends. In all cases the WH consistently retaining a larger bound core compared to the BH for the same β .

C. Critical Impact Parameter

We characterize the transition between partial and full disruption using the critical periaapsis distance $r_{p,c}$ (smallest periaapsis for which a self-bound core survives) or, equivalently the critical impact parameter $\beta_c \equiv r_t/r_{p,c}$. Figure 3 shows that in both spacetimes, $r_{p,c}$ decreases with increasing mass, but WHs consistently exhibit smaller $r_{p,c}$ than BHs, indicating stars can penetrate deeper before complete disruption.

Correspondingly, WHs exhibit systematically larger β_c at all masses. We perform power-law fits for both the critical pericenter and the critical impact parameter. For the critical pericenter, we obtain $r_{p,c}/r_g = 75.50 \times (M_\bullet/10^6 M_\odot)^{-0.89}$ for the BH, and $r_{p,c}/r_g = 76.72 \times (M_\bullet/10^6 M_\odot)^{-0.96}$ for the other case. Similarly, for the critical impact parameter, we find $\beta_c = 0.63 \times (M_\bullet/10^6 M_\odot)^{0.23}$ for the BH, and $\beta_c = 0.62 \times (M_\bullet/10^6 M_\odot)^{0.30}$ for the WH case.

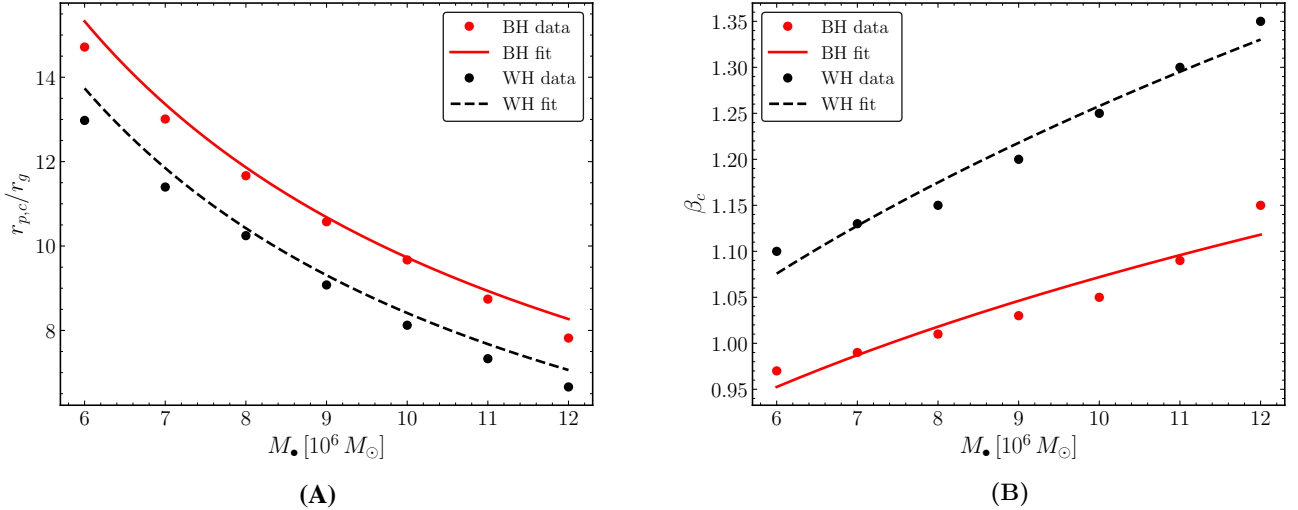


FIG. 3: Critical periapsis distance and critical impact parameter as functions of the BH and WH mass, M_\bullet , shown in units of $10^6 M_\odot$. Panel (A) shows the critical periapsis distance, $r_{p,c}/r_g$, and panel (B) shows the critical impact parameter, β_c , for the BH and WH cases. The red points and solid curves correspond to the BH data and fit, while the black points and dashed curves correspond to the WH data and fit, respectively.

D. Fallback rates

We now study aspects of the fallback rates of debris into the BH or the WH. These are expected to mimic observed light curves from TDEs. Figure 4 shows the fallback rate in our system by compact object of masses $M_\bullet = 6 \times 10^6 M_\odot$ and $M_\bullet = 1.1 \times 10^7 M_\odot$ with impact parameters $\beta = 1.0$ ($r_p \approx 14.2r_g$) and $\beta = 1.1$ ($r_p \approx 9.2r_g$) respectively. The results presented here are obtained within the frozen-in approximation. In this approximation, the debris energy distribution once established, is assumed to remain unchanged thereafter. We have checked in a few cases that fallback rate obtained from the frozen-in approximation is in excellent agreement with those from hydrodynamical simulations, although the latter often involves substantial computation costs.

For the BH case, the disruption is full, i.e., no bound stellar core survives the encounter. In

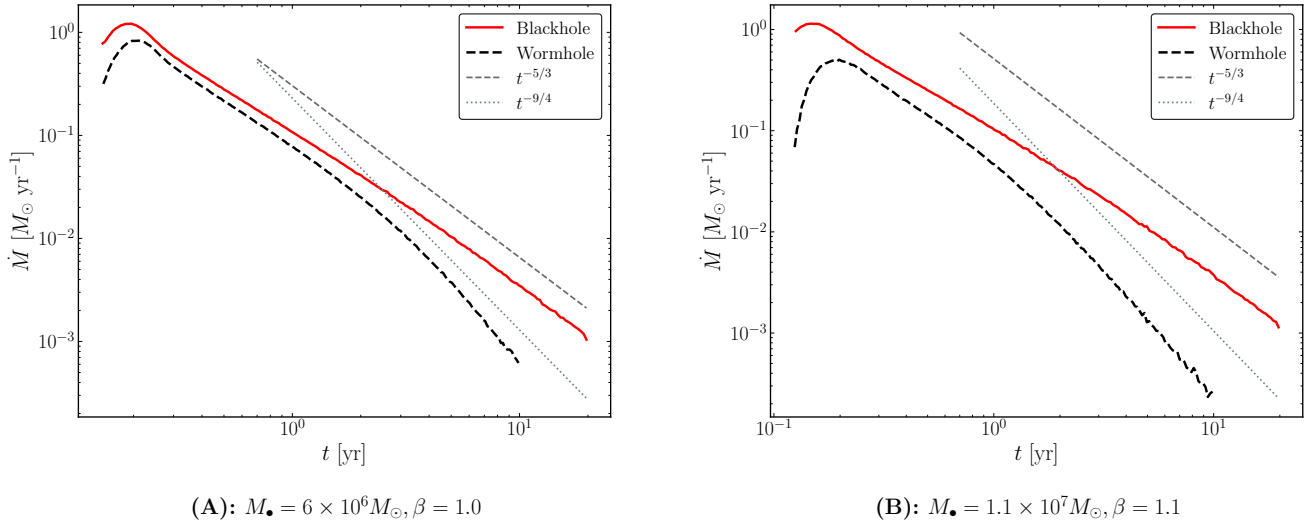


FIG. 4: Fallback rate, \dot{M} , as a function of time, t , for BH (solid red) and WH (dashed black) cases. Panel (A) corresponds to $M_{\bullet} = 6 \times 10^6 M_{\odot}$, $\beta = 1.0$, and panel (B) to $M_{\bullet} = 1.1 \times 10^7 M_{\odot}$, $\beta = 1.1$, with reference slopes $t^{-5/3}$ and $t^{-9/4}$ shown.

The WH case exhibits a steeper late-time decay compared to the BH.

contrast, the WH case results in partial disruption, with approximately 52% of the stellar core remaining gravitationally bound. This qualitative difference in the disruption outcome is directly reflected in the structure of the fallback curves. Note that the BH case exhibits a higher peak fallback rate compared to the WH case. The peak is also marginally earlier in time. At late times, the BH fallback curve follows the usual canonical $t^{-5/3}$ power-law decline expected for a full disruption[14], consistent with the standard analytical prediction. By contrast, the WH curve exhibits a steeper decay, closer to $t^{-9/4}$ as indicated in the figure which was predicted by [46] in partial disruption cases. This comparison demonstrates that, even for identical M_{\bullet} and β , the spacetime geometry strongly influences the disruption outcome and the subsequent fallback evolution.

The behaviour of the fallback rate is explained by differential mass distribution of stellar debris. In Figure 5, the differential mass distribution $dM/d\epsilon$ is plotted as a function of the specific energy in units of $\Delta\epsilon = \frac{GM_{\bullet}R_{*}}{r_t^2}$, for the same values of parameters used in Figure 4. From this figure, we see that the WH exhibits a clear dip at $\epsilon \simeq 0$ in contrast to the BH case. Since the core particles have been removed prior to constructing the histogram, any deficit near zero energy implies that a substantial fraction of mass remains concentrated in a bound, compact core that does not contribute to the debris distribution. The dip therefore signals a partial disruption, where a significant remnant core survives the tidal encounter.

In contrast, the BH case does not exhibit such a dip, since this corresponds to a full TDE, i.e., the entire stellar mass is dispersed into tidal debris. An important feature of Figure 5 is the difference in the

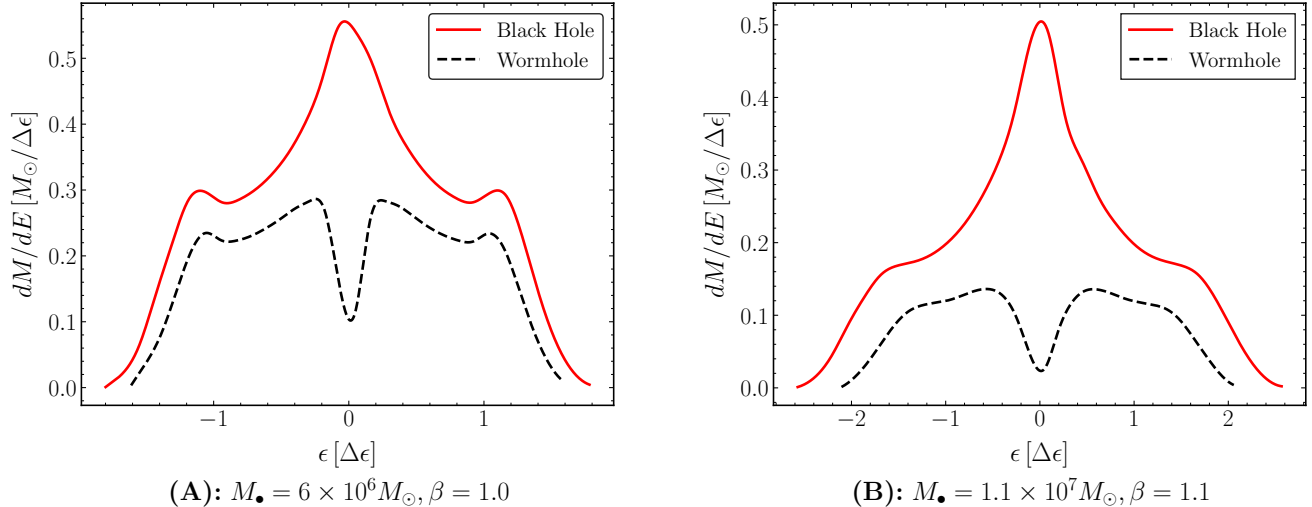


FIG. 5: Energy distribution, $dM/d\epsilon$, as a function of normalized energy, $\epsilon/\Delta\epsilon$, for the BH (solid red) and WH (dashed black) cases. Panel (A) corresponds to $M_{\bullet} = 6 \times 10^6 M_{\odot}$, $\beta = 1.0$, and panel (B) to $M_{\bullet} = 1.1 \times 10^7 M_{\odot}$, $\beta = 1.1$. The WH case shows a suppressed and split distribution near $\epsilon \sim 0$, while the BH case remains more centrally peaked.

overall width of the energy distribution between the BH and WH cases, and this directly relates to our discussion in section IB, see Eq. (7). As discussed there, the BH produces a noticeably broader $dM/d\epsilon$ indicating a larger spread in specific orbital energies imparted to the stellar debris during the disruption. In contrast, the WH distribution is narrower, implying that the debris occupies a more restricted range of energies. A broader energy distribution, as seen in the BH cases, implies the presence of more tightly bound material. Consequently, the most-bound debris in the BH spacetime returns in shorter timescales, leading to an earlier and higher peak in the fallback rate. In contrast, the narrower energy spread in the WH case indicates that fewer debris elements achieve large binding energies. The most-bound material is therefore less tightly bound than in the BH case, resulting in a longer return time for the earliest fallback and a reduced peak accretion rate.

E. Gravitational wave emission from tidal encounters

We now compare Gravitational wave (GW) emission between BH and WH backgrounds. GW emission from TDEs arises from the time-varying quadrupole moment during the star's periapsis passage [47]. The characteristic GW frequency associated with a TDE is set by the dynamical timescale at periapsis,

$$f_{\text{GW}} \sim \left(\frac{GM_{\bullet}}{r_t^3} \right)^{1/2} \sim 6 \times 10^{-4} \text{ Hz } \beta^{3/2} \left(\frac{M_{*}}{M_{\odot}} \right)^{1/2} \left(\frac{R_{*}}{R_{\odot}} \right)^{-3/2}, \quad (10)$$

while the strain amplitude at luminosity distance d_L is:

$$h_{\text{GW}} \sim 2 \times 10^{-22} \beta \left(\frac{M_{\bullet}}{10^6 M_{\odot}} \right)^{2/3} \left(\frac{M_{*}}{M_{\odot}} \right)^{4/3} \left(\frac{R_{*}}{R_{\odot}} \right)^{-1} \left(\frac{d_L}{10 \text{ Mpc}} \right)^{-1}. \quad (11)$$

This estimate confirms that TDE GW signals are intrinsically weak but increase in strength for deep encounters and nearby sources.

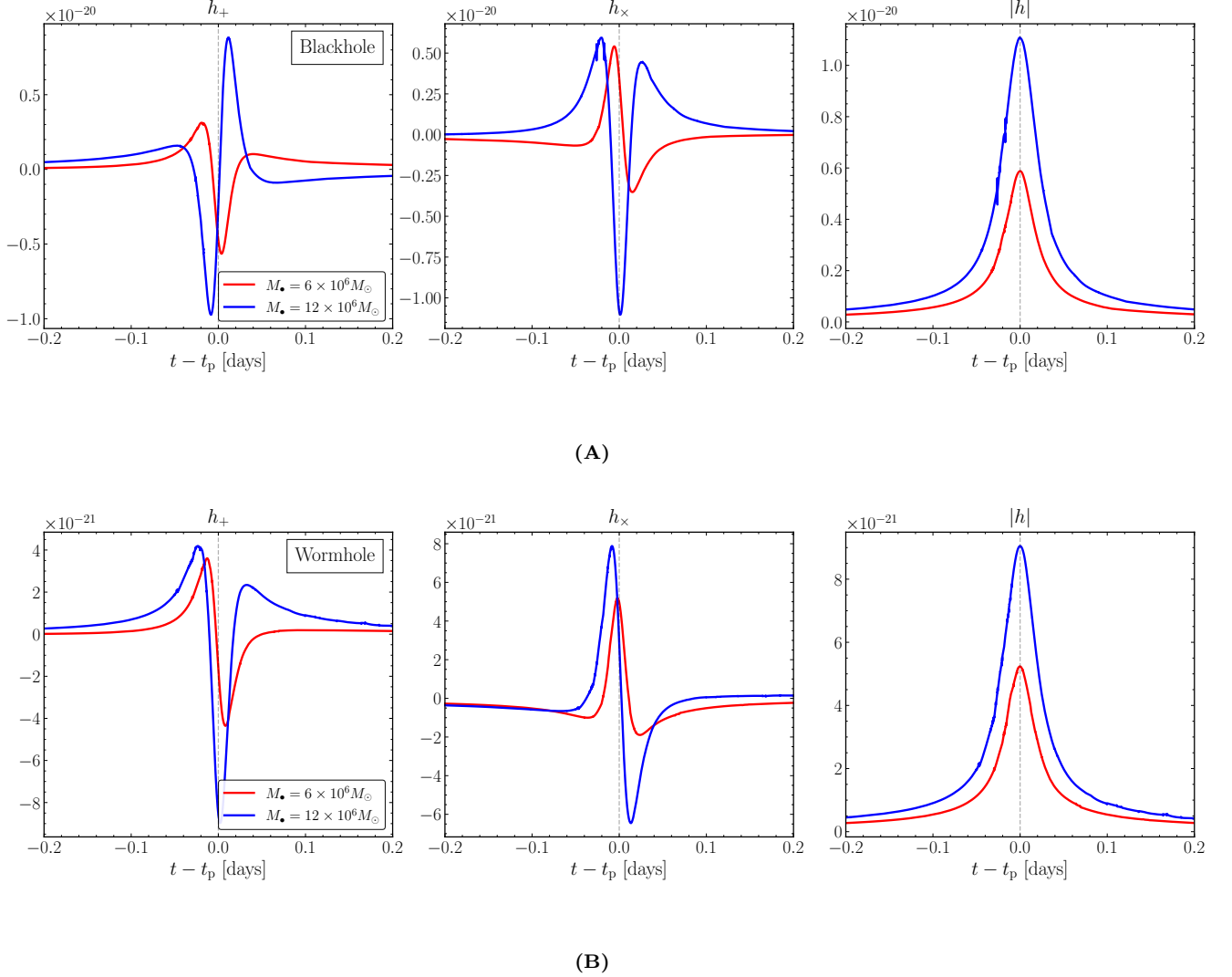


FIG. 6: Gravitational wave strain components, h_+ and h_{\times} , and total strain amplitude $|h|$, as functions of $(t - t_p)$ for face-on inclination, obtained from our simulations at $\beta = 1.1$. Each row displays three panels corresponding to h_+ (left), h_{\times} (middle), and $|h|$ (right). In both cases the red and blue curves correspond to $M_{\bullet} = 6.0 \times 10^6 M_{\odot}$ and $M_{\bullet} = 1.2 \times 10^7 M_{\odot}$, respectively. (a) BH case: The peak amplitude occurs near periastron, with higher mass producing a stronger and sharper GW signal. (b) WH case: Similar to the BH case, the signal peaks near periastron, but the WH shows slightly lower amplitude.

For deep encounters with $\beta \gtrsim 1$ and periastron distances approaching the gravitational radius,

relativistic effects become increasingly important. In the post-Newtonian (PN) framework developed by [48], the waveform is expressed in terms of radiative mass and current multipole moments, which differ from their Newtonian counterparts due to relativistic corrections. In our analysis, these effects are incorporated by consistently including 1PN corrections to the orbital motion when estimating the GW strain and frequency, ensuring validity for moderately relativistic TDE encounters. At leading PN accuracy, the dominant contribution to GW emission arises from the radiative mass quadrupole moment which is, following Eq. (1.3b) of [48], given by

$$\begin{aligned}
I_{ij}^{\text{rad}}(t) &= \int d^3\mathbf{x} \hat{x}_{ij} c^{-2} [T^{00}(\mathbf{x}, t) + T^{ss}(\mathbf{x}, t)] \\
&+ \frac{1}{14c^2} \frac{d^2}{dt^2} \int d^3\mathbf{x} \hat{x}_{ij} \mathbf{x}^2 c^{-2} [T^{00}(\mathbf{x}, t) + T^{ss}(\mathbf{x}, t)] \\
&- \frac{20}{21c^2} \frac{d}{dt} \int d^3\mathbf{x} \hat{x}_{k(i} x_{j)} T^{0k}(\mathbf{x}, t) + \mathcal{O}(c^{-4}),
\end{aligned} \tag{12}$$

where $T^{\mu\nu}$ is the stress–energy tensor of the material source expressed in harmonic coordinates, angular brackets denote the symmetric trace-free (STF) projection, and \hat{x}_{ij} denotes the STF part of $x_i x_j$. For tidal disruption events, the stress–energy tensor corresponds to the evolving stellar debris, whose rapid deformation near periapsis leads to a strongly time-dependent radiative quadrupole moment. While the Newtonian contribution dominates for shallow encounters, the 1PN corrections become increasingly relevant for deep encounters with $\beta \gtrsim 1$, where relativistic velocities are attained.

For an observer located along the z -axis, the two GW polarizations are given by

$$h_+(t) = \frac{G}{c^4 D} \left[\ddot{I}_{xx}^{\text{rad}}(t) - \ddot{I}_{yy}^{\text{rad}}(t) \right], \quad h_\times(t) = \frac{2G}{c^4 D} \ddot{I}_{xy}^{\text{rad}}(t). \tag{13}$$

These expressions remain valid to 1PN accuracy provided the radiative quadrupole moment includes the PN corrections given in Eq. (12).

In Figure 6A, we show the GW polarizations h_+ and h_\times as well as the amplitude $|h| = \sqrt{h_+^2 + h_\times^2}$ for the $6 \times 10^6 M_\odot$ and $1.2 \times 10^7 M_\odot$ BHs for the face-on inclination. Figure 6B shows these for the corresponding same-mass WHs in the same inclination. All the figures are plotted for $\beta = 1.1$, for which the background with mass $6 \times 10^6 M_\odot$ results in full disruption in both cases whereas both backgrounds result in partial disruption for mass $1.2 \times 10^7 M_\odot$. From the figures, we see that the behaviour of $|h|$ is qualitatively similar for both the BH and WH backgrounds, with only a change in amplitude observed at the same order.

IV. COMPARISON WITH PREVIOUS STUDIES

Prior to our work, the authors of [49] performed a suite of fully relativistic hydrodynamic simulations

of tidal disruptions of main sequence stars by SMBHs, in a Schwarzschild spacetime, using a different numerical recipe than ours. In their setup, the BH spacetime and tidal field are treated relativistically, while the star’s self gravity is computed via a Newtonian Poisson solver in a comoving local tetrad frame, where the metric is approximately Minkowski. The stellar potential is then added to g_{tt} in that local frame as a post-Newtonian correction. Further, they define a “physical tidal radius” \mathcal{R}_t , as the maximum periapsis distance at which full disruption occurs, and show that this is enhanced relative to the Newtonian tidal radius r_t (of Eq. 1). For partial disruptions, they find that the remnant mass fraction M_{rem}/M_* at a given normalized periapsis r_p/\mathcal{R}_t increases with M_\bullet .

In our work, we have also considered back-reaction due to star’s gravity as a small linear perturbation to the background metric, following [50]. By solving the relativistic fluid equations, we get a velocity-dependent self-gravity correction of the form

$$\mathbf{a}_{\text{sg}} = -U^0 \left(1 - \frac{\delta_{lm} v^l v^m}{c^2} \right) \nabla \Phi_{\text{sg}} , \quad (14)$$

where U^0 is the gravitational time-dilation factor, v is the local three-velocity in the fluid frame, and Φ_{sg} is the self gravitational potential of the star.

In the deep relativistic regime ($\beta \gtrsim 0.95$, large M_\bullet), [49] finds that for a fixed normalized periapsis r_p/\mathcal{R}_t , the remnant mass fraction increases with M_\bullet : stars hold on to more of their mass when the encounter is more relativistic. They attribute this to relativistic modifications of the tidal tensor and debris dynamics, not to any change in self-gravity. In our framework, as M_\bullet grows and β increases, the periapsis velocity approaches c and the factor $(1 - v^2/c^2)$ becomes small, weakening self-gravity. Naively, this might suggest even a stronger disruption. However, our simulations show that at sufficiently deep encounters the qualitative trend remains the same, i.e., for fixed $r_p/r_{p,c}$, the surviving core mass fraction increases with M_\bullet , and the critical impact parameter β_c for full disruption rises.

The difference of our results from treating hydrodynamics in the Newtonian regime can be explained from the fact that geodesic congruence effects in relativistic tidal fields compete with, and eventually dominate over, the weakening of self gravity. Nearby fluid elements in the star follow a bundle of timelike geodesics whose separation is governed by the geodesic deviation equation. This geodesic convergence leads to stronger tangential compression than in the Newtonian case and naturally produces a very dense core that is effectively decoupled from the large scale tidal field. This is in close analogy with the core survival found in [51] for underluminous TDEs.

At the same time, gravitational time dilation reduces the proper frame duration of the periapsis passage. The proper time interval experienced by the star during the strongest part of the encounter is shorter by a factor $\sqrt{1 - r_s/r}$ than the coordinate time. Our explicit orbit integrations show that, for the deep relativistic encounters we consider, the proper crossing time at periapsis becomes comparable

to, or smaller than, the stellar sound crossing time. Pressure gradients and tidal counterforces therefore have very little proper time to deform or unbind the innermost region. The inner core is compressed and then exits periapsis essentially ballistically, with its structure largely preserved.

To better understand the reason behind stars retaining a larger bound core mass for higher BH mass, we calculate the tidal potential as experienced by the star at the periapsis. We consider the local FN basis inside which the star co-rotates with its orbital motion (the “tilde frame” in which the computations of section IB were also done). While this is an assumption that does not hold true throughout the parabolic geodesic of the stellar core, the star is mostly tidally locked at the periapsis. As a result, the co-rotating frame is a good assumption there. We calculate the tidal potential in the FN frame, which increases with distance from the centre of mass (COM) of the star (the origin of the FN frame). We track the magnitude of the tidal potential along the BH direction (ϕ_x) and along the two other perpendicular directions (ϕ_y and ϕ_z). While the tidal force field acts towards expanding the star towards the BH or WH (and away from it), in the other two perpendicular directions, the tidal field compresses the stellar body. We calculate the magnitude of the tidal potential at a distance $1R_\odot$ from the COM. We repeat this task for higher ADM masses. We find that the magnitude of tidal potential increases with ADM mass.

In Figure 7, we show change of tidal potential in the FN set up described above with increasing ADM mass. Since the tidal potential is zero at the COM of the star, and its value at the surface of the star ($1R_\odot$) increases with BH mass, it is evident that the corresponding tidal force (compressing force) also increases with ADM mass. Therefore, we expect that the star will be able to retain more core mass in the case of a higher ADM mass in TDEs that show partial disruptions. From the same figure we also plot tidal potential at $r_{p,c}$ with increasing ADM mass. It supports our earlier observation that post TDE remnant core retains more mass for WH spacetime than that of BH spacetime. In this sense, our study can be viewed as an extension of the work of [49] that incorporates a physically motivated modification of stellar self-gravity. From both of hydrodynamic simulation and FNC calculation we quantify how the disruption efficiency and critical impact parameter $\beta_c(M)$ change. The critical periapsis distance normalized by the gravitational radius of the BH decreases approximately twice as rapidly in our case compared to that reported in [49]. This indicates that a proper relativistic treatment requires a deeper encounter to achieve the same degree of tidal disruption.

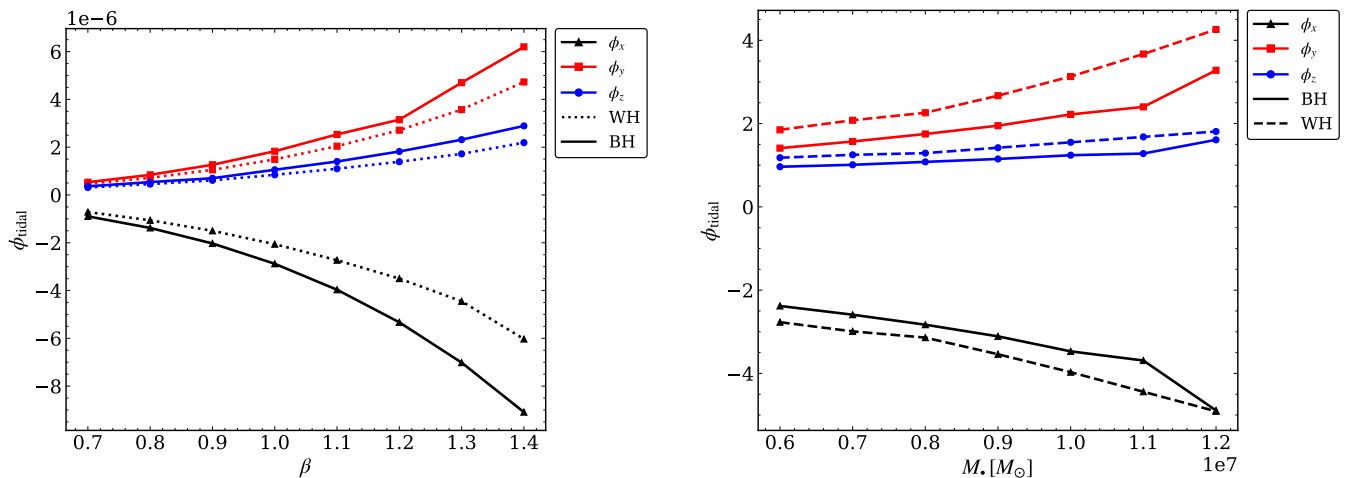


FIG. 7: Tidal potential components, ϕ_x , ϕ_y , and ϕ_z , for BH (solid) and WH (dashed) cases. The left panel shows ϕ_{tidal} as a function of the impact parameter β for $M_\bullet = 10^7 M_\odot$, while the right panel shows ϕ_{tidal} at $r_{p,c}$ as a function of M_\bullet . The WH case exhibits systematically weaker tidal compression compared to the BH, particularly in the ϕ_x component.

V. COMPACTNESS AS A MEASURE OF TIDAL DISRUPTION IN THE RELATIVISTIC REGIME

To quantify the outcome of close stellar encounters, we construct a compactness parameter from the tidal force evaluated at periapsis in the FN frame. The radial tidal field ϕ_x represents the relativistic tidal stretching responsible for unbinding stellar material, while ϕ_y and ϕ_z encode stabilizing transverse compression that supports core survival. A natural geometric measure of the competition between these effects is provided by the anisotropy ratio

$$\mathcal{A} = \frac{\sqrt{\phi_y^2 + \phi_z^2}}{|\phi_x|}, \quad (15)$$

which depends only on the relative magnitudes of the tidal eigenvalues and therefore captures relativistic effects arising from the underlying spacetime geometry.

Tidal disruption, however, is not determined by anisotropy alone. The strength of the encounter is controlled by the impact parameter β . In the Newtonian limit, the magnitude of the tidal field at periapsis scales as

$$|\lambda_x| \sim \frac{GM_\bullet R_*}{r_p^3} = \beta^3 \frac{GM_*}{R_*^2}. \quad (16)$$

The factor β^3 thus represents the Newtonian amplification of tidal strength associated with deeper encounters and is independent of the local anisotropy of the tidal tensor.

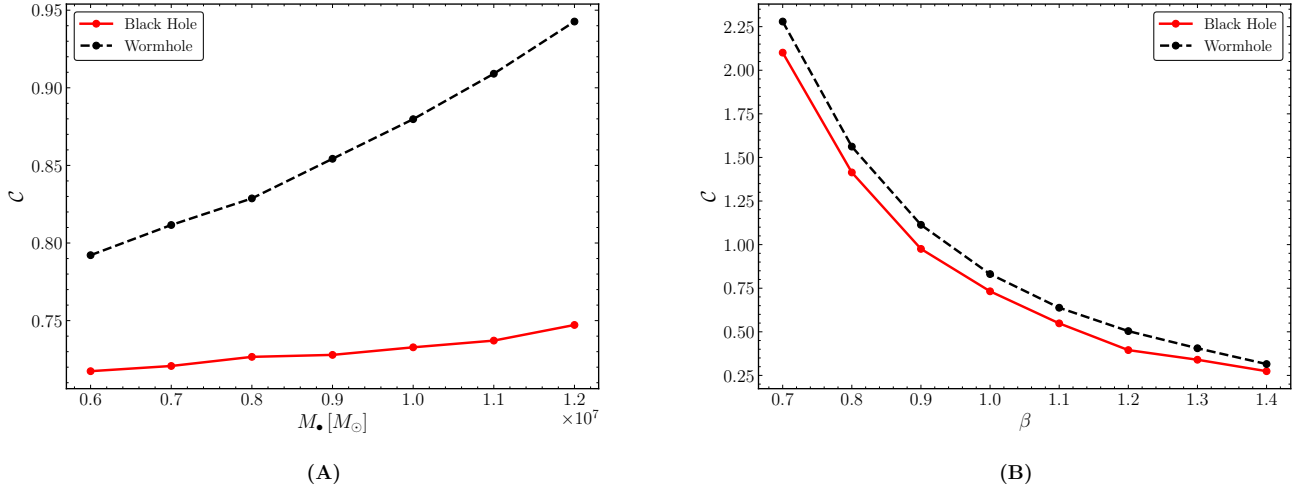


FIG. 8: Compactness, C , of the star for BH (solid red) and WH (dashed black) cases. The left panel shows C as a function of M_\bullet at fixed $\beta = 1$, while the right panel shows C as a function of β for $M_\bullet = 10^7 M_\odot$. In both cases, the WH yields a higher compactness than the BH, with C decreasing as β increases.

Motivated by these considerations, we define the compactness parameter as

$$\mathcal{C} = \frac{\sqrt{\phi_y^2 + \phi_z^2}}{|\phi_x| \beta^3}. \quad (17)$$

This definition cleanly separates the physical origins of the two contributions: the ratio of tidal eigenvalues encodes relativistic tidal anisotropy through the FN frame, while the explicit β^3 factor incorporates the Newtonian scaling of tidal strength with periapsis distance.

For a fixed impact parameter ($\beta = 1$), the compactness reduces to $\mathcal{C} = \mathcal{A}$ and depends solely on the geometry of the tidal field. In this regime, increasing the mass of the central object leads to a more isotropic tidal configuration, enhancing transverse compression relative to radial stretching and thereby increasing the compactness Figure 8(A). This behaviour explains why higher-mass central objects tend to retain a larger fraction of stellar material for encounters of identical depth. For fixed central mass and varying impact parameter, the β^3 dependence dominates the behaviour of \mathcal{C} . As β increases, the rapid growth of tidal strength overwhelms the stabilizing transverse compression, leading to a sharp decrease in compactness and enhanced disruption Figure 8(B). This trend reflects the increasing dominance of tidal work over stellar self-gravity in deep encounters.

A comparison between BH and WH spacetimes shows that WHs systematically exhibit larger compactness values across both parameter scans, indicating weaker disruption efficiency. This difference originates from relativistic modifications of the tidal eigenvalues ϕ_i in the WH geometry, which enhance transverse compression relative to radial stretching. The compactness defined in Eq. 17 therefore provides

a unified and physically motivated diagnostic for comparing tidal disruption outcomes across different spacetimes and encounter regimes.

In summary, the results presented in Figure 8(A) demonstrate that, for a fixed impact parameter β_c , the stellar compactness increases with increasing mass of the central compact object. This qualitative trend is consistent with our finding that the critical impact parameter β_c increases with BH or WH mass. In other words, more massive compact objects require deeper encounters (larger β) to achieve complete disruption. The Figure 8(B) further shows that, for a fixed central mass, the stellar compactness decreases rapidly with increasing β , as expected. Deeper encounters enhance tidal deformation and mass stripping, thereby reducing the bound core and lowering the remnant compactness. Finally, we find that, for identical values of mass and β , WH spacetimes consistently produce higher post-encounter stellar compactness compared to BHs. This indicates that tidal interactions in WH geometries are comparatively less efficient at fully disrupting the star, leading to a more tightly bound remnant under otherwise identical orbital parameters.

VI. DISCUSSIONS AND CONCLUSIONS

It is well known by now that WHs might be horizonless BH mimickers. This makes it important and interesting to study dynamics in these backgrounds, and astrophysical tidal disruption events are very well suited to carry out this analysis. Although these have been studied before using static methods where one transforms to a locally inertial FN frame, a comparative analysis disruption dynamics using numerical simulations is not available in the literature. In this paper we fill this gap and present a number of novel results that arise from simulations of solar mass stars in supermassive BH or WH backgrounds. In particular, using general relativistic smoothed particle hydrodynamics, we probe deep encounters, i.e., strong gravity regimes in these. This is an important feature of our analysis, as similar mass BHs and WHs essentially behave like similar Newtonian masses for mild encounters.

To begin with, we have shown that due to the inherently different spacetime geometry, WHs retain substantially more self-bound mass than BHs in partial disruptions. This led us to a discussion on the critical impact parameter β_c that separates the region of full disruption from partial ones. We have quantified how this is consistently higher for the WH, as compared to the BH, due to the weaker gravity of the former even in deep regimes. Further, we have shown that β_c increases with BH or WH mass, and explained this by a FN frame computation. We have also commented upon the distribution of energy in stellar debris and discussed GWs in both backgrounds.

Before we end this paper, we make a few important comments. Firstly, it might be prudent to ask if one can, in some sense, “distinguish between” BHs and their mimickers from observational data. To

this end, note that the gravitational wave signal from a TDE encodes information about the binary interaction (M, M_*, R_*, β) through the characteristic frequencies, strain amplitudes and their temporal evolution. See, for example, Eqs (10), (11), and the expressions for the frequency and amplitude of GWs generated via strong compression near periapsis, given by [13] :

$$f_{\text{comp}} \simeq 4 \times 10^{-5} \beta^4 \left(\frac{M_*}{M_\odot}\right)^{1/2} \left(\frac{R_*}{R_\odot}\right)^{-3/2} \text{ Hz} \quad (18)$$

$$h_{\text{comp}} \simeq 10^{-27} \beta^2 \left(\frac{M_*}{M_\odot}\right)^2 \left(\frac{R_*}{R_\odot}\right)^{-1} \left(\frac{d_L}{20 \text{ Mpc}}\right)^{-1}. \quad (19)$$

We also assume that we have a given mass radius relation of the stellar object, and that the observer distance d_L is known (see below). In an ideal scenario, if one estimates the 4 parameters from the above constraints, the TDE observables, when compared with the observed data, directly indicate whether the data prefer a BH model or a WH model. For example, having the estimated values of M, M_*, R_*, β from GW, the detection of a late-time fallback rate scaling $\sim \dot{M} \propto t^{-9/4}$, rather than the canonical $t^{-5/3}$ expected for a full tidal disruption, may indicate a deviation from the standard Schwarzschild BH scenario and is potentially consistent with a static exponential WH. However, given the fact that f_{comp} and h_{comp} in Eqs (18) and (19) are orders of magnitude less than that of Eqs. (10) and (11), they might turn out to be insufficient to estimate all the 4 parameters. In that case, one might have to utilise both GW and TDE constraints simultaneously for a Bayesian model selection. For the latter case, we need the analytical prescriptions for the peak fall-back rate \dot{M}_{peak} which occurs at time t_{peak} , and the fitting expression for the fall-back rate as a function of time $\dot{M}_{\text{fit}}(t)$ (which includes the late-time behaviour) for both partial and full TDEs for both BHs and WHs and for a given star and its evolutionary stage. One such approach to obtain the analytical formulas is given in [43] and [52]. A relativistic extension of their study is required in order to implement the analytical models into the statistical analysis for our case.

In order to substantiate our argument regarding the mass-radius relation and the observer distance d_L , we further note that the spectroscopic classification of TDEs provides direct evidence for determining whether the disrupted star was on the main sequence or in an evolved stage. TDE-H events, which exhibit strong hydrogen Balmer emission lines, indicate disruption of main-sequence stars that retain their hydrogen-rich envelopes [53, 54]. In contrast, TDE-He events dominated by helium lines with minimal hydrogen signatures suggest the disruption of evolved stars that have shed their hydrogen envelopes, such as helium cores or stripped stars [53]. One might use spectroscopic data from TDEs to determine whether the disrupted star is a main-sequence star and, hence, use the appropriate mass-radius relation. Also, from the EM wave redshift and GW redshift, we can estimate d_L .

We also note that the fallback rate is used as an observable in our study. However, the real observable is the luminosity of a TDE. The fallback rate determines the rate at which debris falls towards the

BH or WH, creating an accretion disk. The accretion process leads to the observed luminosity. The accretion efficiency depends on the viscous timescale, which is expected to be much shorter than the fallback timescale in the early stages of fallback (days to a few months) [58, 59]. Therefore, the peak fallback is expected to lead the TDE light curve. The late-time behaviour, on the other hand, is primarily determined by the viscous timescale, making it challenging to follow the late-time slope of the fallback. Therefore, we emphasize that the entire fallback analytical model has to be utilized in the Bayesian analysis. Secondly, the t_{peak} used in our analysis measures the peak fallback time from the start of the simulation. In reality, the peak time can only be measured from the detection of the first light, which is the time t_{fd} taken by the most bound debris to return to the pericenter and drive the accretion-induced emission. Therefore, we need to use t_{fd} as an additional parameter in the Bayesian analysis.

Finally, we emphasise here that we have taken a particular example of a horizonless compact object, namely the exponential WH. It is therefore natural to ask if our results are generic. In this context, we recall that this particular example was chosen in order to avoid interactions between ‘exotic’ matter due to the WH and stellar debris, that would make an SPH analysis more challenging. If we do not consider such interactions and assume only gravitational interactions of stellar debris, then our results should remain robust for other WH backgrounds as well, as borne out by a local FN frame analysis.

ACKNOWLEDGMENTS

We acknowledge the support and resources provided by PARAM Sanganak under the National Supercomputing Mission, Government of India, at the Indian Institute of Technology Kanpur.

DATA AVAILABILITY STATEMENT

The data underlying this article will be shared upon reasonable request to the corresponding author.

Appendix A: Numerical tests

Here, we present the standard test results achieved by our general relativistic smoothed particle hydrodynamics code. We arrange the numerical tests in two parts: one for special relativity and another for general relativity.

1. Tests of Special Relativity

In this section, we show the results obtained using our code for the following tests: 3D relativistic shock tube, 1D blast wave, 1D and 3D sinusoidal shock tube, transverse shock tube and radial oscillation of a polytropic star. All tests have been performed in $c = G = 1$ units, with artificial viscosity parameter $\alpha_{AV} = 1$ and artificial conductivity $\alpha_u = 0.1$ unless otherwise stated. All figures in this subsection are generated using SPLASH.

a. 3D shock tube test

We perform this test for a fluid with 72012 particles with the following initial condition:

$$[\rho, P] = \begin{cases} [10, 13.33333] & \text{for } x < 0 \\ [1.125, 0.000001] & \text{for } x > 0 \end{cases} \quad (\text{A1})$$

The maximum Lorentz factor achieved in this test is $\Gamma \sim 1.4$.

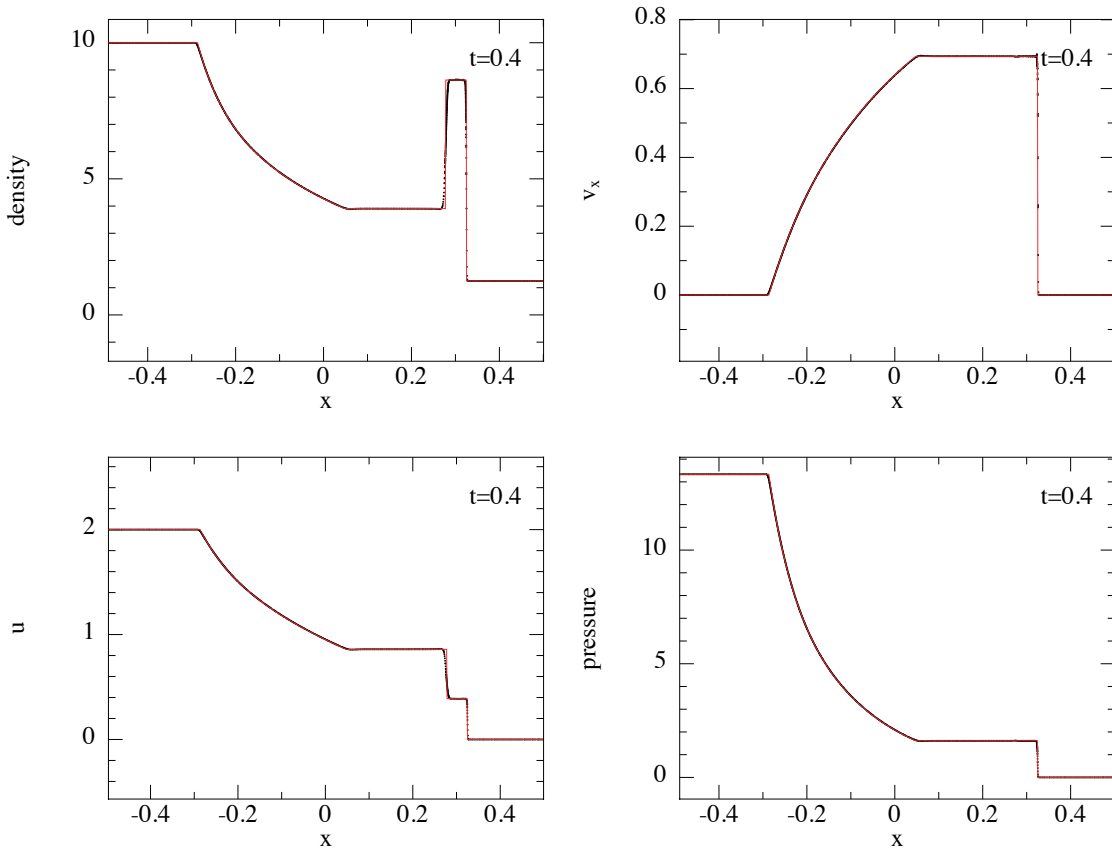


FIG. 9: 3D shock tube test. Black circles show SPH particles, while the red line represents the analytical solution.

b. 1D blast wave test

The Blast-wave test has been performed in 1D. The particle separation is 0.0001 on both sides of the interface. This test achieved a maximum Lorentz factor of 3.6. For the initial configuration, we use the following set up:

$$[\rho, P] = \begin{cases} [1, 1000] & \text{for } x < 0 \\ [1, 0.001] & \text{for } x > 0 \end{cases} \quad (\text{A2})$$

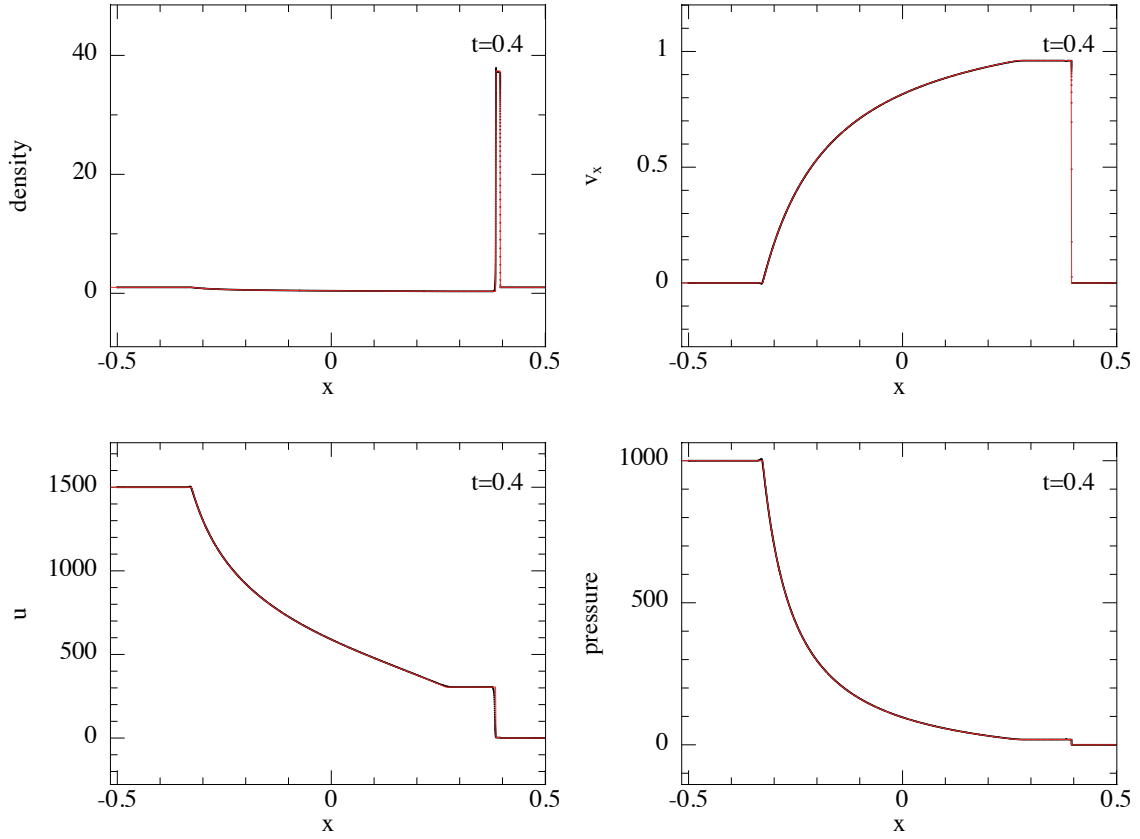


FIG. 10: 1D blast wave test. Black circles denote SPH particles, while the red line shows the analytical solution from Martí and Müller [56].

c. 1D sinusoidal shock tube test

Here, we perform a 1D shock tube with a sinusoidally perturbed density distribution in the right-hand side $x > 0$. The maximum value of the Lorentz factor reached is $\Gamma = 1.15$. The initial condition we used

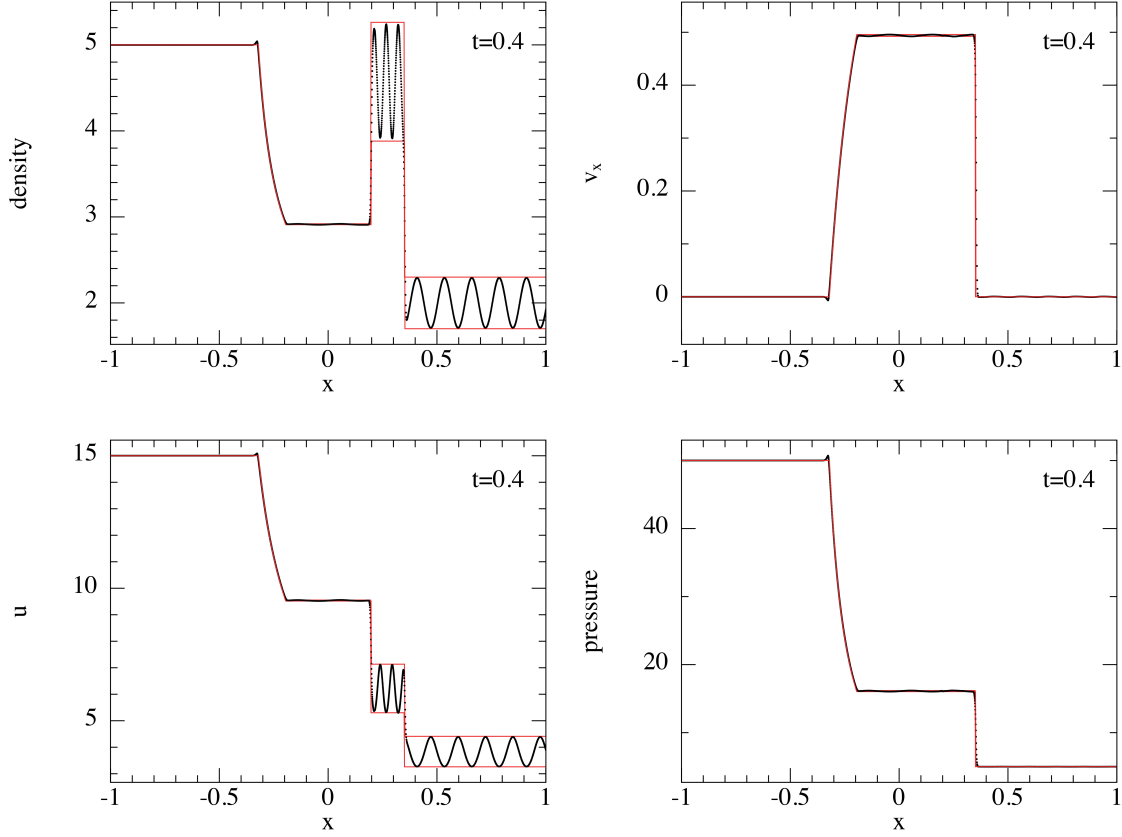


FIG. 11: 1D sinusoidally perturbed shock tube test. Black circles denote SPH particles, while the red curves represent analytical solutions corresponding to the upper and lower density extremes of the sine perturbation.

for this setup is

$$[\rho, P] = \begin{cases} [5, 50] & \text{for } x < 0 \\ [2 + 0.3 \sin(50x), 5] & \text{for } x > 0 \end{cases} \quad (\text{A3})$$

The test has been performed with 7001 particles. From the simulation results, we see that the sine-wave perturbation is accurately preserved across the shock front. The peaks of the propagated sine wave are consistent with the limiting analytical solutions.

d. 3D sinusoidal shock tube test

Here, we perform a 3D shock tube test with a sinusoidally perturbed density state on the right hand side. The maximum value of the Lorentz factor reached by the fluid is $\Gamma = 1.15$. The initial conditions we used for this setup are

$$[\rho, P] = \begin{cases} [8, 50] & \text{for } x < 0 \\ [1 + 0.3 \sin(50x), 5] & \text{for } x > 0 \end{cases} \quad (\text{A4})$$

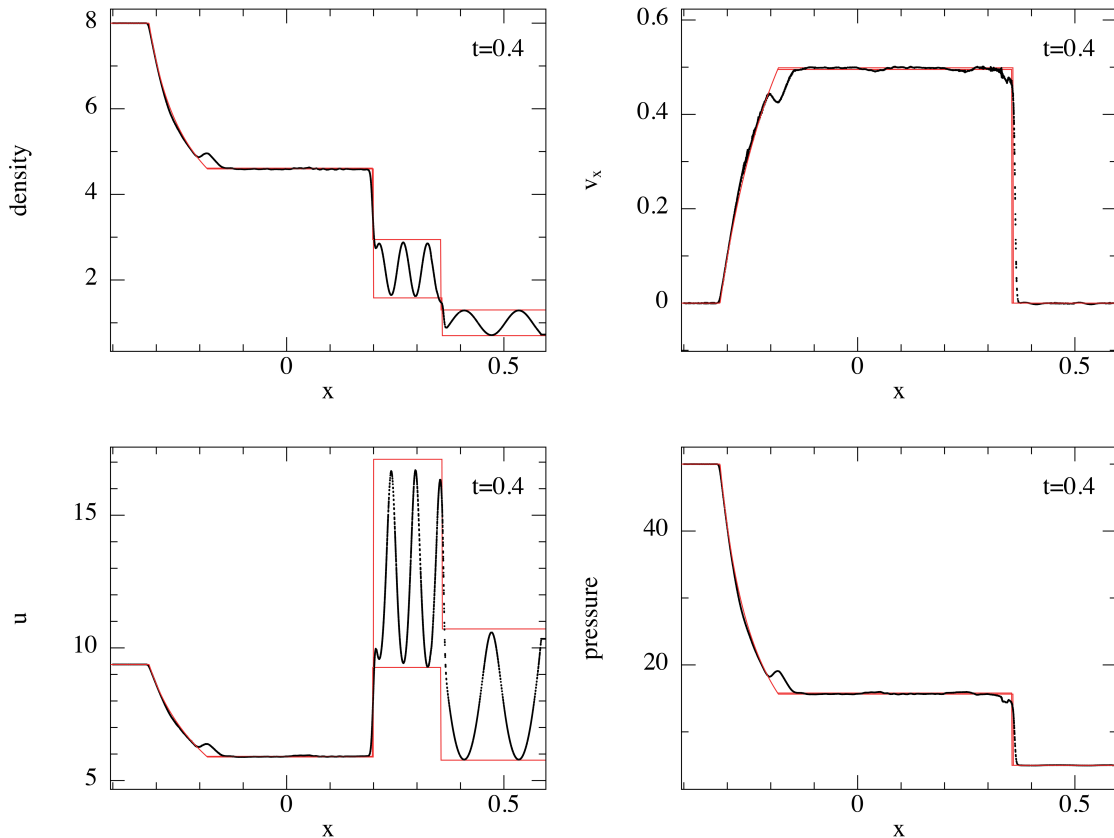


FIG. 12: 3D sinusoidally perturbed shock tube test. Black circles denote SPH particles, while the red curves represent analytical solutions corresponding to the upper and lower density extremes of the sine perturbation.

This test has been performed with a total 76097 particles. From the simulation results, we observe a consistent pattern with the 1D sine-wave shock tube test.

e. 3D transverse shock tube test

In the transverse shock tube test, we consider that the fluid in the $x > 0$ region has a relativistic transverse velocity. The magnitude of flow speed is constrained in relativistic flow by the speed of light. Also, transverse velocity is coupled to the evolution of the other hydrodynamic quantities through the Lorentz factor. Using the following initial conditions, we perform this test using 199996 particles. The fluid achieves a maximum Lorentz factor $\Gamma \sim 9.0$.

$$[\rho, P, v_x, v_y] = \begin{cases} [1, 1000, 0, 0] & \text{for } x < 0 \\ [1, 0.01, 0, 0.9938] & \text{for } x > 0 \end{cases} \quad (\text{A5})$$

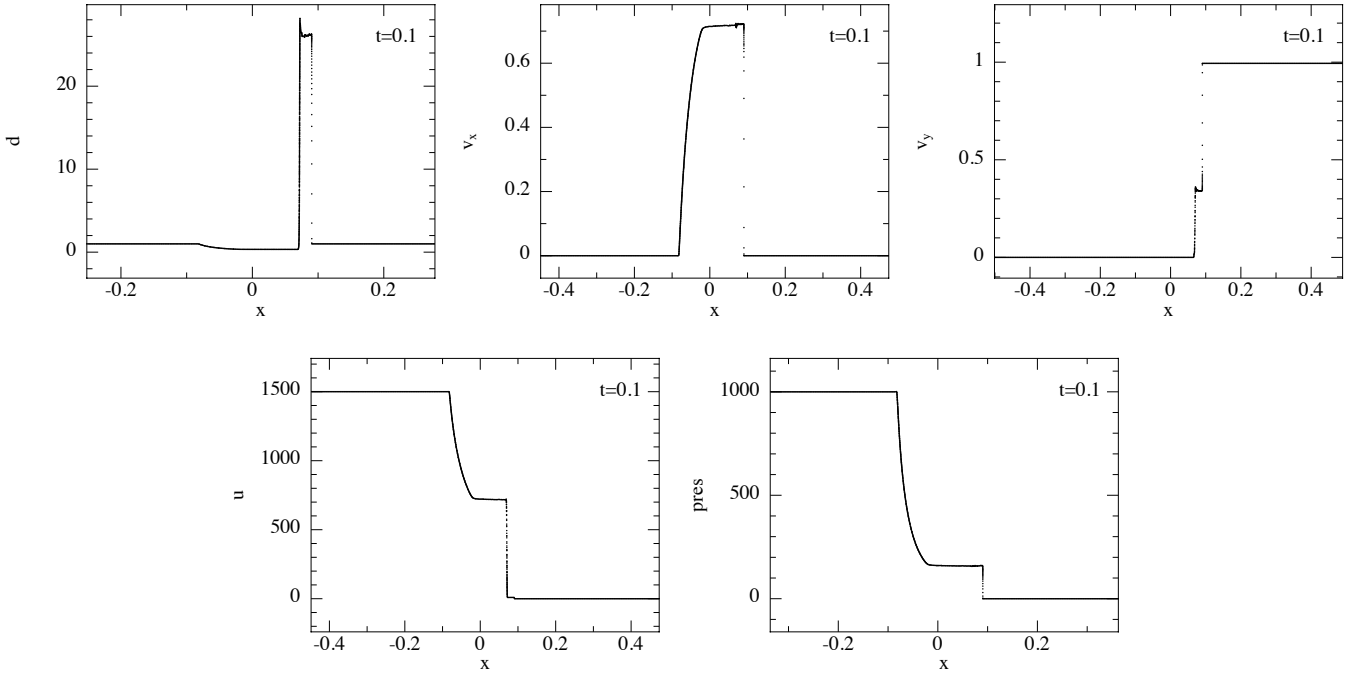


FIG. 13: Transverse shock tube test has been performed in 3D, The black circles show the SPH particles.

2. Tests of General Relativity

a. Geodesic test

In order to study the ability of our code to simulate orbital dynamics, we test it for the Schwarzschild and Morris-Thorne exponential WH metric in Cartesian coordinates. To match geodesics, we have taken a test star of $1 M_{\odot}$, $0.1 R_{\odot}$ and $\gamma = 2$. The eccentricity and the impact parameter are 0.85 and 0.6 respectively, for both cases.

b. Radial Velocity

To test the behaviour of the radial velocity, we consider a compact star of mass $1 M_{\odot}$ and radius $0.1 R_{\odot}$ on a parabolic orbit with impact parameter $\beta = 0.9$ in the gravitational field of a $10^6 M_{\odot}$ BH. Figure 15A and a WH spacetime Figure 15B. For these parameters, tidal disruption is negligible, allowing the star to be treated as a test object even in the strong gravity regime.

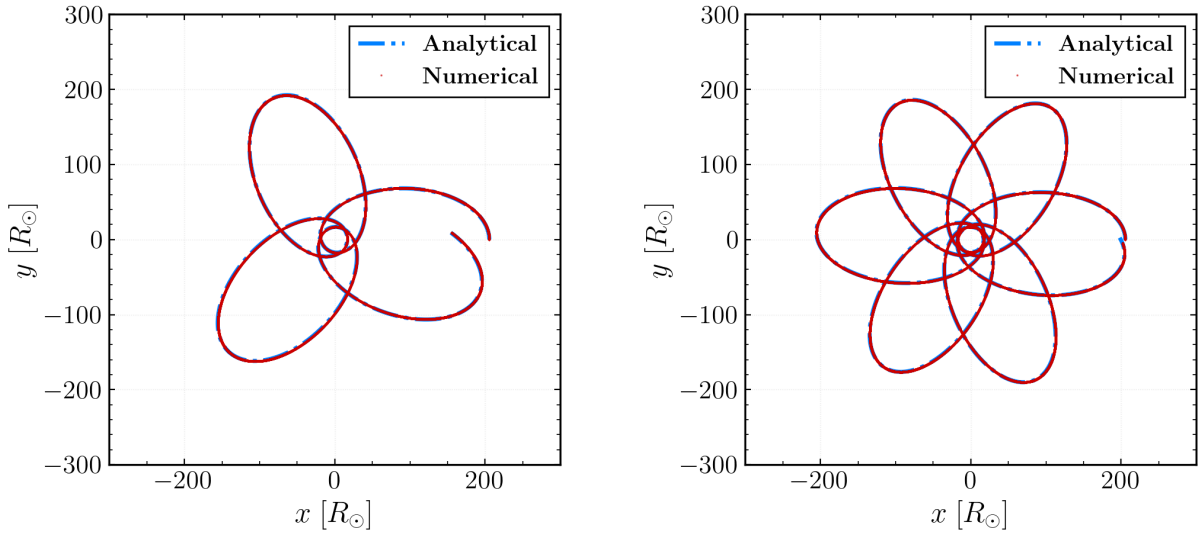


FIG. 14: On left panel: orbit around BH. On right panel: orbit around WH

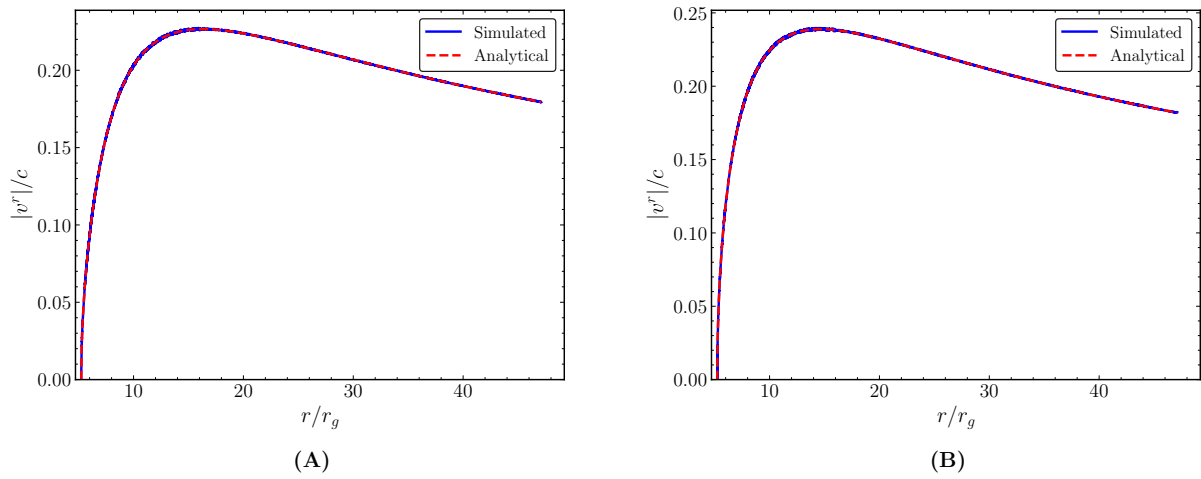


FIG. 15: Radial velocity test in the Schwarzschild BH background (A) and the exponential WH background (B).

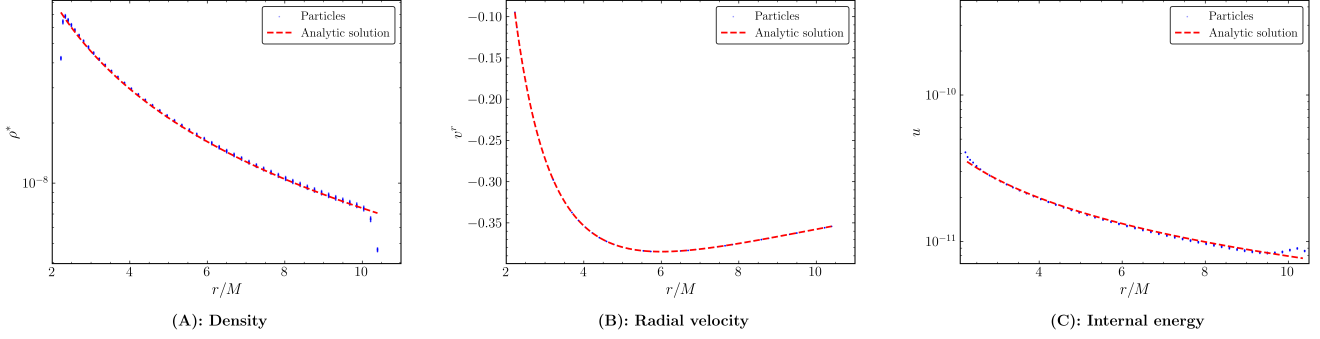


FIG. 16: Bondi geodesic test with $\alpha = 0$ at $t = 55$ code units.

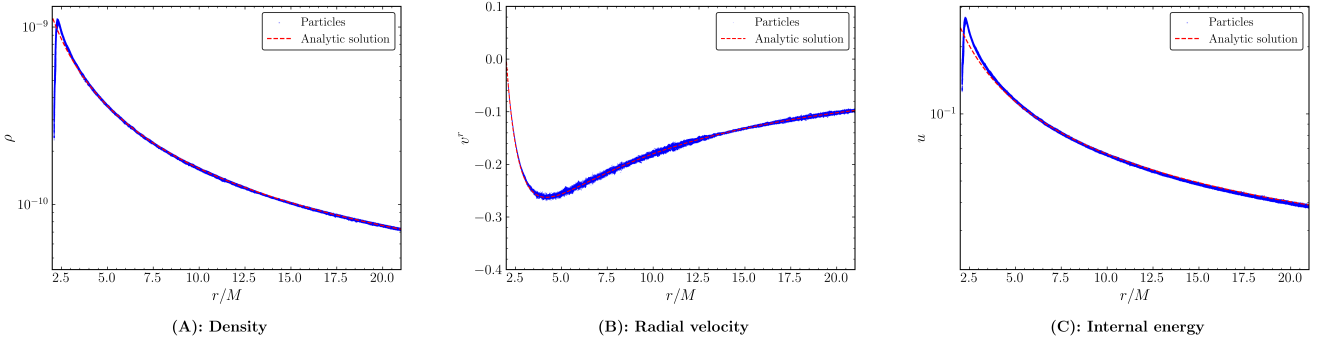


FIG. 17: Sonic flow test with $\alpha = 0.3$ at $t = 577$ code units.

c. Bondi accretion for a pressure-less gas

To test Bondi accretion for a pressure-less gas, we have taken the solution given by [55]

$$v^r(r) = \sqrt{\frac{2M_\bullet}{r}} \left(1 - \frac{2M_\bullet}{r}\right) \quad (\text{A6})$$

$$\rho(r) = \frac{\rho_0}{r^2} \sqrt{\frac{r}{2M_\bullet}} \quad (\text{A7})$$

$$u(r) = u_0 \left(r^2 \sqrt{\frac{2M_\bullet}{r}} \right)^{1-\gamma_{\text{ad}}} \quad (\text{A8})$$

where ρ_0 and u_0 are normalization constants. We have taken $\rho_0 = 3.35 \times 10^{-7}$, $M_\bullet = 1$ and $u_0 = 10^{-10}$. We keep 50 shells of 14400 particles with mass $1.4 \times 10^{-10} M_\bullet$ outside $r_{\text{in}} = 20M_\bullet$ distance, each shell is kept at $0.5M_\bullet$ temporal distance. Keeping the $\alpha_{\text{AV}} = 0$ we let the system evolve. We have shown the density and radial velocity profile in Figure 16. We have used the $G = c = 1$ units for this test.

d. Bondi sonic flow test

To perform the sonic flow test, we follow the solution outlined in [57]. In our simulation, we filled the region from $r = 2.2M_{\bullet}$ to $r = 22M_{\bullet}$ with spherical shells, with 5400 particles per shell, with each particle mass $1.0 \times 10^{-11}M_{\bullet}$ with $M_{\bullet} = 1$. Each shell is kept at a time interval dt from the previous one. We choose $dt = 1.3M_{\bullet}$, critical point $r_c = 8M_{\bullet}$ and $\gamma = 5/3$. We continuously inject shells at dt time intervals. For the simulation, we have taken $\alpha = 0.3$, $\alpha_u = 0.1$ and $G = c = 1$. The simulation result at $t = 577$ code units is shown in Figure 17.

-
- [1] M.J. Rees, *Tidal disruption of stars by black holes of $10^6 - 10^8$ solar masses in nearby galaxies*, *Nature* **333** (1988) 523.
 - [2] E.S. Phinney, *The Galactic Center*, in *IAU Symp.* **136**, ed. M. Morris (1989) 543.
 - [3] J.M. Lattimer and D.N. Schramm, *The tidal disruption of a neutron star by a black hole*, *Astrophys. J.* **210** (1976) 549.
 - [4] C.R. Evans and C.S. Kochanek, *The tidal disruption of a star by a black hole*, *Astrophys. J.* **346** (1989) L13.
 - [5] D. Syer and A. Ulmer, *The fallback of debris in the tidal disruption of a star*, *MNRAS* **306** (1999) 35.
 - [6] J. Magorrian and S. Tremaine, *The rates of stellar disruption by massive black holes*, *MNRAS* **309** (1999) 447.
 - [7] H. Shiokawa et al., *General Relativistic Hydrodynamic Simulation of Accretion Flow from a Stellar Tidal Disruption*, *Astrophys. J.* **804** (2015) 85 [1501.04365].
 - [8] P.G. Jonker et al., *The Tidal Disruption of Stars by Massive Black Holes*, *Space Sci. Rev.* **216** (2020) 124.
 - [9] R. Genzel, F. Eisenhauer and S. Gillessen, *The Galactic Center massive black hole*, *Rev. Mod. Phys.* **82** (2010) 3121 [1006.0064].
 - [10] J. Kormendy and L.C. Ho, *Coevolution of Supermassive Black Holes and Host Galaxies*, *Ann. Rev. Astron. Astrophys.* **51** (2013) 511 [1304.7762].
 - [11] T. Alexander, *Stellar Dynamics and Stellar Phenomena Near Massive Black Holes*, *Ann. Rev. Astron. Astrophys.* **55** (2017) 1 [1701.04762].
 - [12] J. Guillochon and E. Ramirez-Ruiz, *Hydrodynamical simulations to determine the feeding rate of black holes by the tidal disruption of stars*, *Astrophys. J.* **767** (2013) 25 [1206.2350].
 - [13] N.C. Stone et al., *Stellar Tidal Disruption Events in General Relativity*, *Gen. Rel. Grav.* **51** (2019) 30 [1801.10180].

- [14] G. Lodato, A.R. King and J.E. Pringle, *Stellar disruption by a supermassive black hole: is the light curve really proportional to $t^{-5/3}$?*, *MNRAS* **392** (2009) 332 [0810.1288].
- [15] G. Lodato and E.M. Rossi, *Multiband light curves of tidal disruption events*, *MNRAS* **410** (2011) 359 [1008.4589].
- [16] B.D. Metzger and N.C. Stone, *A bright year for tidal disruptions*, *MNRAS* **461** (2016) 948.
- [17] S. van Velzen et al., *A radio jet from the optical and x-ray tidal disruption flare ASASSN-14li*, *Science* **351** (2016) 62 [1511.08803].
- [18] M. Kesden, *Black-hole spin dependence in the light curves of tidal disruption events*, *Phys. Rev. D* **86** (2012) 064026 [1207.6401].
- [19] C. Misner and J.A. Wheeler, *Classical physics as geometry*, *Ann. Phys.* **2** (1957) 525.
- [20] K. Sato et al., *Multi-Production of Quasars from a Giant Cosmological Wormhole*, *Prog. Theor. Phys.* **65** (1981) 1443.
- [21] H. Kodama et al., *Creation of Wormholes by LMR in the Early Universe*, *Prog. Theor. Phys.* **66** (1981) 2052.
- [22] K. Maeda et al., *The expansion of a giant cosmological wormhole*, *Phys. Lett. B* **108** (1982) 98.
- [23] R.W. Fuller and J.A. Wheeler, *Causality and Multiply Connected Space-Time*, *Phys. Rev.* **128** (1962) 919.
- [24] M.S. Morris and K.S. Thorne, *Wormholes in spacetime and their use for interstellar travel*, *Am. J. Phys.* **56** (1988) 395.
- [25] M.S. Morris, K.S. Thorne and U. Yurtsever, *Wormholes, Time Machines, and the Weak Energy Condition*, *Phys. Rev. Lett.* **61** (1988) 1446.
- [26] I.D. Novikov, *An analysis of the operation of a time machine*, *JETP* **95** (1989) 769.
- [27] M. Visser, *Lorentzian Wormholes: From Einstein to Hawking*, Woodbury, USA (1995).
- [28] J.P.S. Lemos, F.S.N. Lobo and S. Quinet de Oliveira, *Morris-Thorne wormholes with a cosmological constant*, *Phys. Rev. D* **68** (2003) 064004 [gr-qc/0302049].
- [29] S. Kar and D. Sahdev, *Euclidean wormholes with non-minimal coupling*, *Phys. Rev. D* **53** (1996) 722.
- [30] F.S.N. Lobo and M.A. Oliveira, *Evolving Lorentzian wormholes*, *Phys. Rev. D* **80** (2010) 104012 [0909.5539].
- [31] T. Damour and S.N. Solodukhin, *Wormholes as black hole foils*, *Phys. Rev. D* **76** (2007) 024016 [0704.2667].
- [32] V. Cardoso, E. Franzin, and P. Pani, *Is the Gravitational-Wave Ringdown a Probe of the Event Horizon?*, *Phys. Rev. Lett.* **116** (2016) 171101 [1602.07309].
- [33] R.A. Konoplya and A. Zhidenko, *Wormholes versus black holes: quasinormal ringing at early and late times*, *JCAP* **12** (2016) 043 [1606.00517].

- [34] P. Banerjee et al., *Tidal disruption near black holes and their mimickers*, *JCAP* **03** (2021) 042 [1912.01184].
- [35] M. Ishii, M. Shibata and Y. Mino, *Black hole tidal problem in the fermi normal coordinates*, *Phys. Rev. D* **71** (2005) 044017 [gr-qc/0501084].
- [36] M. Ishii, M. Shibata, *Numerical Study of the Tidal Disruption of Neutron Stars Moving around a Black Hole: — Compressible Jeans and Roche Problems*, *Prog. Theor. Phys.* **112** no. 3, 399 (2004).
- [37] M. Shibata, K. Taniguchi, *Merger of black hole and neutron star in general relativity: Tidal disruption, torus mass, and gravitational waves* *Phys. Rev.* **D77**, 084015 (2008) [0711.1410].
- [38] M. Kesden, *Tidal-disruption rate of stars by spinning supermassive black holes* *Phys. Rev.* **D85**, 024037 (2012) [1109.6329].
- [39] D. Garain and T. Sarkar, *Partial tidal disruptions of spinning eccentric white dwarfs by spinning intermediate-mass black holes*, *Mon. Not. Roy. Astron. Soc.* **542**, no.2, 839-856 (2025), [2401.17031].
- [40] D. Liptai and D. J. Price, *General relativistic smoothed particle hydrodynamics*, *Mon. Not. Roy. Astron. Soc.* **485**, no.1, 819-842 (2019) [1901.08064].
- [41] D. Liptai, D. J. Price, I. Mandel and G. Lodato, *Disc formation from tidal disruption of stars on eccentric orbits by Kerr black holes using GRSPH*, [1910.10154].
- [42] D. Mainetti, A. Lupi, S. Campana, M. Colpi, E.R. Coughlin, J. Guillochon and E. Ramirez-Ruiz, *The fine line between total and partial tidal disruption events*, *Astron. Astrophys.* **600** (2017) A45 [1702.07730].
- [43] E.R. Coughlin, C.J. Nixon *A simple and accurate prescription for the tidal disruption radius of a star and the peak accretion rate in tidal disruption events*, *Mon. Not. Roy. Astron. Soc. Lett.* **517** (2022) L26 [2208.13788].
- [44] E. Gafton, E. Tejada, J. Guillochon, O. Korobkin and S. Rosswog, *Relativistic effects on tidal disruption kicks of solitary stars*, *Mon. Not. Roy. Astron. Soc.* **449** (2015) 771 [1502.02039].
- [45] R. M. Cheng and C. R. Evans, *Relativistic effects in the tidal interaction between a white dwarf and a massive black hole in Fermi normal coordinates*, *Phys. Rev. D* **87**, no.10, 104010 (2013) [1303.4129].
- [46] P.R. Miles, N. C. Stone, E. R. Coughlin and A. Bonnerot, *Fallback Rates from Partial Tidal Disruption Events*, *Astrophys. J.* **899** (2020) 36 [2006.09375].
- [47] P. C. Peters and J. Mathews, *Gravitational Radiation from Point Masses in a Keplerian Orbit*, *Phys. Rev.* **131** (1963) 435.
- [48] L. Blanchet and T. Damour, *Radiative gravitational fields in general relativity I. General structure of the field outside the source*, *Ann. Inst. H. Poincaré Phys. Théor.* **50** (1989) 377.
- [49] T. Ryu, J. Krolik, T. Piran and S.C. Noble, *Tidal Disruptions of Main-sequence Stars. IV. Relativistic Effects and Dependence on Black Hole Mass*, *Astrophys. J.* **904** (2020) 101.

- [50] D. Liptai, *General relativistic smoothed particle hydrodynamics with application to the tidal disruption of stars by supermassive black holes*, Monash University PhD Thesis (2020).
- [51] P. Amaro-Seoane, *Underluminous tidal disruption events*, *Mon. Not. Roy. Astron. Soc.* **533** (2024) 1233 [2307.13043].
- [52] A. Bandopadhyay, E.R. Coughlin and C.J. Nixon, *The Maximum Gravity Model for partial Tidal Disruption Events: Mass Loss, Peak fallback Rate and Dependence on Stellar Properties*, [2601.02476].
- [53] S. Gezari *et al.*, *An ultraviolet-optical flare from the tidal disruption of a helium-rich stellar core*, *Nature* **485** (2012) 217 [1205.0252].
- [54] I. Arcavi *et al.*, *A Continuum of H- to He-rich Tidal Disruption Candidates With a Preference for E+A Galaxies*, *Astrophys. J.* **793** (2014) 38 [1405.1415].
- [55] J. F. Hawley, L. L. Smarr and J. R. Wilson, *A numerical study of nonspherical black hole accretion. I. Equations and test problems*, *Astrophys. J.* **277** (1984) 296.
- [56] J.M. Martí and E. Müller, *The analytical solution of the Riemann problem in relativistic hydrodynamics*, *J. Fluid Mech.* **258** (1994) 317–333.
- [57] F. C. Michel, *Accretion of matter by condensed objects*, *Astrophys. Space Sci.* **15** (1972) 153.
- [58] B. Mockler, J. Guillochon and E. Ramirez-Ruiz, *Weighing Black Holes Using Tidal Disruption Events*, *Astrophys. J.* **872** (2019) 151.
- [59] M. Nicholl, D. Lanning, P. Ramsden, B. Mockler, A. Lawrence, P. Short and E. J. Ridley, *Systematic light-curve modelling of TDEs: statistical differences between the spectroscopic classes*, *Mon. Not. R. Astron. Soc.* **515** (2022) 5604.